universität wien

MASTERARBEIT / MASTER'S THESIS

Titel der Masterarbeit / Title of the Master's Thesis

The Antiproton Annihilation Experiment at ASACUSA using a Timepix3 detector

verfasst von / submitted by

Melanie Strube, BSc

angestrebter akademischer Grad / in partial fulfilment of the requirements for the degree of

Master of Science (MSc)

Wien, 2019 / Vienna, 2019

Studienkennzahl lt. Studienblatt / degree programme code as it appears on the student record sheet:	A A 066 876
Studienrichtung lt. Studienblatt / degree programme as it appears on the student record sheet:	Masterstudium Physik
Betreut von / Supervisor:	Dr. Johann Zmeskal, Privatdoz.

Zusammenfassung

Die Multiplizitätsverteilungen von geladenen Sekundärteilchen (Pionen, Protonen, Alphateilchen und andere Kernfragmente) für niederenergetische Antiprotonenannihilationen sind kaum bekannt. Sie sind aber ein wichtiger Bestandteil von Monte-Carlo Simulationen, welche z.B. den Hintergrund bei Antimaterie-Experimenten modellieren sollen.
Solche Simulationen werden heutzutage hauptsächlich mit den Software-Paketen CHIPS, FLUKA und FRITIOF durchgeführt. Diese Pakete wurden für Anwendungen in der Hochenergiephysik geschrieben. Simulationen im niederenergetischen Bereich werden entsprechend extrapoliert.
Bis vor einigen Jahren gab es keine experimentellen Messdaten von Antiproton-Nukleus Annihilationen in diesem Energiebereich ($<1\,\mathrm{keV}$), wodurch die genannten Modelle nicht validiert werden konnten. Erste Vergleiche zeigen, dass keines der 3 Pakete niederenergetische Annihilationen befriedigend modelliert.

Die ASACUSA (Atomic Spectroscopy And Collisions Using Slow Antiprotons) Collaboration führte Ende 2017 eine systematische Studie von Annihilationen niederenergetischer Antiprotonen an einer dünnen Kohlenstoff-Folie durch. Die vorhandene Beamline wurde um eine elektrostatische Linse (Steerer lens) erweitert. Ein Bismut-Germanat (BGO) Detektor des Antiwasserstoff-Experiments wurde für dieses Experiment durch einen Timepix3-Pixeldetektor ersetzt.
Im Rahmen dieser Masterarbeit wurden einige der Neuerungen vor ihrem Einsatz getestet. Auch wurden Messungen des Magnetfeldes vor Ort am CERN durchgeführt, welche in zukünftige Simulationen einfließen sollten, sowie ein erster Blick auf die Daten, welche mit Timepix3 aufgezeichnet wurden, geboten.

Abstract

The multiplicity distribution of charged annihilation products (pions, protons, alpha particles and other nuclear fragments) is not well known for antiprotons annihilating at rest on nuclei. However, this information is important for Monte-Carlo simulations to model the background for antimatter experiments.
Current simulations are being performed mainly with the CHIPS, FLUKA or FRITIOF packages. These were written for application in high-energy physics. They extrapolate their data for simulations in the low-energy range.
Up until a few years ago, the absence of experimental data in this range ($<1\,\mathrm{keV}$) made validation of these models difficult. First comparisons show that none of these 3 packages was able to satisfyingly model low-energy annihilations.

At the end of 2017, the ASACUSA (Atomic Spectroscopy And Collisions Using Slow Antiprotons) Collaboration conducted a systematic study of low-energy antiproton annihilations on a thin carbon foil. An electrostatic lens (Steerer lens) was added to the existing beamline. The bismuth germanate (BGO) detector from antihydrogen experiments was replaced with a Timepix3 pixel detector during annihilation studies. In the scope of this thesis, the additions to the beamline were tested before their usage. Some measurements of the magnetic field on-site at CERN were performed to be included in future simulations of the beamline. A first glimpse at the Timepix3 data is also offered.

Contents

1. Introduction

1.1 Motivation

The mechanism by which low energy antiproton annihilations take place is still not very well understood. The multiplicity distribution of Minimum Ionizing Particles (MIPs) and Heavily Ionizing Particles (HIPs) is not well known for antiprotons annihilating at rest on nuclei. This is an important information for Monte Carlo simulations (like GEANT4) to simulate e.g. the background in antimatter experiments.
Current packages for simulations include CHIPS - a quark-level 3D event generator for the fragmentation of excited hadronic systems into individual hadrons [1], FLUKA - which describes hadron-nucleon inelastic collisions in terms of resonance production and decay [2], and FRITIOF - which relies on a string model to describe hadron interactions [3]. These models were developed for high energy physics applications, so none of them use data of annihilations at rest on nuclei. Instead, they are extrapolated to low-energy antiproton annihilations. The lack of low energy antiproton-annihilation data made validating these models difficult in the past.
A few recent experiments show disagreement when compared to low-energy simulations performed with these packages (see [4], [5], Fig. 1.1). Correct simulations are important for planning and analyzing antimatter experiments, so information for improving simulation software is needed. This is why the ASACUSA Collaboration (introduced in 1.2) conducted a systematic study of low-energy antiproton annihilations on a thin carbon foil.

With ELENA (Extra Low ENergy Antiproton ring, [6]) being set to start operation in 2021 and providing antiprotons at even lower energies, new antimatter experiments will be possible. This makes dedicated low-energy experiments on antiproton annihilations for improving simulation software even more topical.

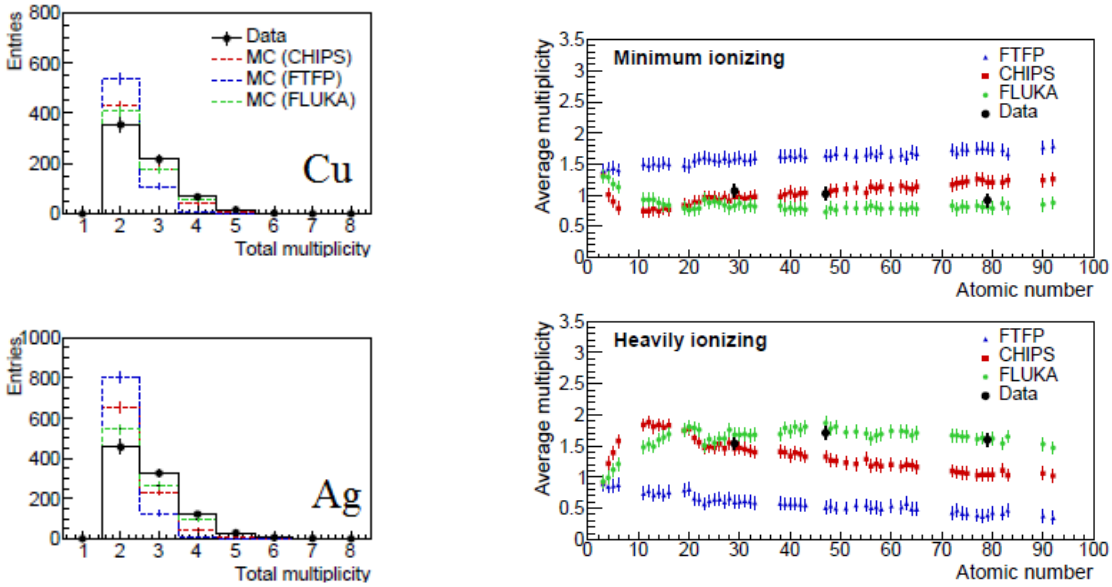

(a) Comparison of the total multiplicities with simulations for copper and silver.

(b) Simulated particle multiplicities of HIPs and MIPs as a function of atomic number, compared with experimental data for Cu, Ag and Au.

Figure 1.1: Graphs comparing the simulated multiplicities for antiproton annihilations with experimental data. One can see that the simulations do not model the experiment accurately, with FLUKA performing slightly better than FTFP (FRITIOF) or CHIPS (graphs taken from [5]).

1.2 ASACUSA collaboration

ASACUSA (Atomic Spectroscopy And Collisions Using Slow Antiprotons) is an international collaboration, its members include institutions from Japan, Austria, Germany, Hungary, Denmark, Italy and CERN. It conducts several antimatter experiments at the Antiproton Decelerator of CERN:

1. Laser spectroscopy of antiprotonic helium to determine the antiproton-to-electron mass-ratio and thus the mass of the antiproton. The proton mass is a well known constant in physics, and any discrepancy between these two values would point at $\mathcal{CPT}$ violation [7].

2. Measuring the ground-state hyperfine structure of antihydrogen via a Rabi-like experiment and comparing it to hydrogen. The hyperfine structure of hydrogen

has been measured with high precision, and as before, a discrepancy between these values would indicate that $\mathcal{CPT}$ symmetry is broken [8].

3. Studying the interactions between matter and antimatter by colliding low-energy antiproton beams with various nuclei (as e.g. this work outlines).

1.3 Theory of antiproton annihilation

This section aims to give a rough overview of past antiproton experiments, as well as a coarse insight into the different theories of antiproton annihilations. Large parts of this section are based on Ref. [9], and more detailed information, especially the mathematics behind the models, can be found in this paper as well as references therein.

Overview of antiproton experiments

The antiproton was discovered in 1955 [10], via the use of one of the first particle accelerators, the Bevatron at Berkeley. The first experiments on antiproton annihilations started in the 1960s and 1970s, the two main experiments were performed at the Brookhaven National Laboratory (BNL) and the Proton Synchrotron at CERN. Extensive experiments were being carried out between 1983 and 1996 at the LEAR (Low Energy Antiproton Ring) at CERN, namely the ASTERIX, OBELIX and Crystal Barrel experiments. ASTERIX mainly measured $\overline{\mathrm{p}}\mathrm{p}$ annihilations in a gaseous H_2 target by observing the resulting X-rays. OBELIX allowed for usage of several different targets (H_2 and D_2, both liquid and gaseous at different pressures) as well as studies of antineutron beams. They had a very broad experimental program, covering atomic, nuclear, and particle physics. Finally, the Crystal Barrel experiment studied $\overline{\mathrm{p}}\mathrm{p}$ and $\overline{\mathrm{p}}\mathrm{n}$ annihilations at rest and in flight. The experiment derives its name from its detector, an electromagnetic calorimeter, shaped like a barrel and made of CsI-crystals.
After the closure of LEAR, its successor, the Antiproton Decelerator (AD) started operation in 2000. It supplies several antimatter experiments, among them ASACUSA.

Antiproton-nucleon annihilation

When a particle comes in contact with its antiparticle, annihilation can occur. This is a process that happens on the level of elementary particles. New particles are created, conserving energy, momentum and charge of the system. Probably the most well-known annihilation process is that of an electron-positron pair at rest, creating two 511 keV photons.

Antiproton annihilations with protons (or neutrons) on the other hand are a far more complex process. Although experiments have been carried out for over more than 50 years, the exact underlying process is still not well understood.
Antiprotons are not elementary particles, they are composite particles made of three quarks ($\overline{uud}$), bound by gluons. When coming into contact with a nucleon, not all quarks necessarily annihilate. This holds especially true for e.g. antiproton-neutron-annihilations, where one of the constituent quarks of the antiproton does not have an "antipartner" in the neutron.
There are different models trying to explain and model the underlying physics of annihilation processes. In the quark rearrangement model for example, the constituent quarks of antiproton and nucleon simply rearrange, forming a final state consisting of three mesons:

$$(\overline{qqq}) + (qqq) \rightarrow (\overline{q}q) + (\overline{q}q) + (\overline{q}q)$$

This model's shortcoming is that it cannot explain processes resulting in 2 mesons in their final state or the production of mesons containing an (anti-)strange-quark, like kaons. For low-energy antiproton-proton annihilations, there exists a non-relativistic quark model [11], combining quark rearrangement and quark-antiquark-annihilation, resulting in 2 mesons in the final state.

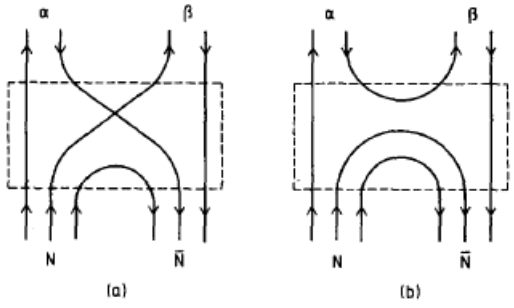

Figure 1.2: Nucleon-antinucleon annihilation resulting in two mesons. (a) shows an annihilation of one quark pair, followed by rearrangement, (b) shows an annihilation of two quarks and a pair creation (image from [11])

The baryon exchange model uses an analogy to electron-positron-annihilation. Where the latter is being mediated by a virtual electron, the antiproton-nucleus-annihilation is mediated via a virtual baryon in the baryon exchange model.
None of these models can fully explain the available data on antiproton annihilations. Especially some *dynamical selection rules*, that is, some obviously suppressed (but kinematically allowed) processes remain puzzling.

Antiproton-nucleus interactions

This following part is a brief summary of Ref. [12]. For more info see this paper and references therein.

The situation becomes even more complex when taking interaction with atomic nuclei into account, as is the case in this experiment. When annihilation occurs, the resulting products can then interact with the rest of the nucleus themselves, causing it to fragment.

The annihilation at rest begins with the capture of a slow antiproton in a Bohr orbit with high principal quantum number, n~40. The so formed antiprotonic atom is highly excited, the antiproton cascades downward, emitting Auger electrons (for high n) and X-rays until it reaches an orbit close to the nucleus, where the strong force kicks in. The antiproton annihilates on the edge of the nucleus, producing (mostly) pions that are emitted isotropically. Some of the pions escape without interacting with the nucleus, while the other pions, themselves interacting strongly, may be absorbed by the nucleus and start an intranuclear cascade. These so-called primordial pions cascade through the nucleus, transferring their energies onto it, and causing the ejection of several nucleons and maybe production of other pions. After the cascading process is finished, the nucleus may still remain with some excitation energy. Some more nucleons may be ejected, or the nucleus may fragment (depends on the nucleus' mass).

2. Experimental setup

2.1 Antiproton production at CERN

For the production of antiprotons, the Proton Synchrotron (PS) at CERN will be used. Here, protons are accelerated and produce antiprotons via the reaction

$$p_{beam} + p_{target} \rightarrow p + p + p + \overline{p} \tag{2.1}$$

After this, the antiprotons enter the Antiproton Decelerator (AD) for cooling and subsequent extraction toward the different experimental beamlines.

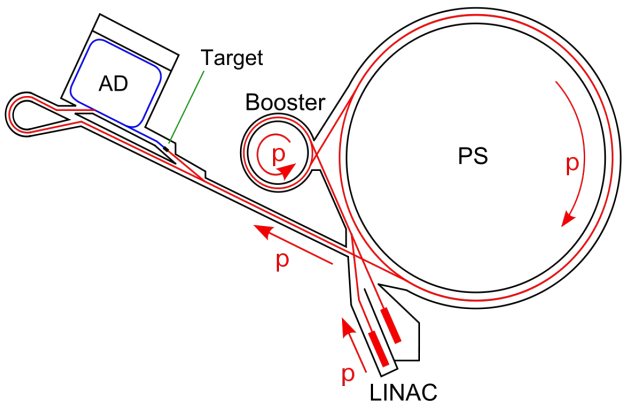

Figure 2.1: The CERN accelerator chain for producing antiprotons. Protons are accelerated by LINAC2, PSB and PS before hitting a target. Resulting antiprotons are guided into the AD. (source: `https://commons.wikimedia.org/w/index.php?curid=7753492`)

The production of antiprotons starts with a bottle of H_2 gas at the Linear accelerator 2 (LINAC2). The hydrogen is stripped of its electrons via an electric field, and the resulting protons enter LINAC2, where they are accelerated to 50 MeV.
Next, the protons enter the Proton Synchrotron Booster (PSB), a synchrotron

accelerator made of four superimposed rings and a circumference of 157 m, and then the Proton Synchrotron (PS), also a synchrotron with a circumference of 628 m, for further acceleration. The PSB accelerates the protons to 1.4 GeV, the PS further to 25 GeV. Then the bunches are steered onto an iridium target. Here, reaction 2.1 takes place, the resulting antiprotons (E ~ 3.6 GeV) are collected by a magnetic horn and focused to the Antiproton Decelerator (AD). Figure 2.1 gives an overview of this whole chain of accelerators.
The AD is a storage ring with a circumference of 188 m. It works "in a reverse mode", so the antiprotons are decelerated instead of accelerated. In several steps, the antiprotons are slowed down to a momentum of 100 MeV/c (kinetic energy ~5 MeV). Every 100 s, a bunch of typically 10^7 antiprotons can then be provided to different experiments. See Figure 2.2 for an overview of the AD hall and experimental area. See also [13] for a more detailed overview of the antiproton accumulation system at CERN and [14] for an overview of the production of low-energy antiprotons and the different experiments at the AD.

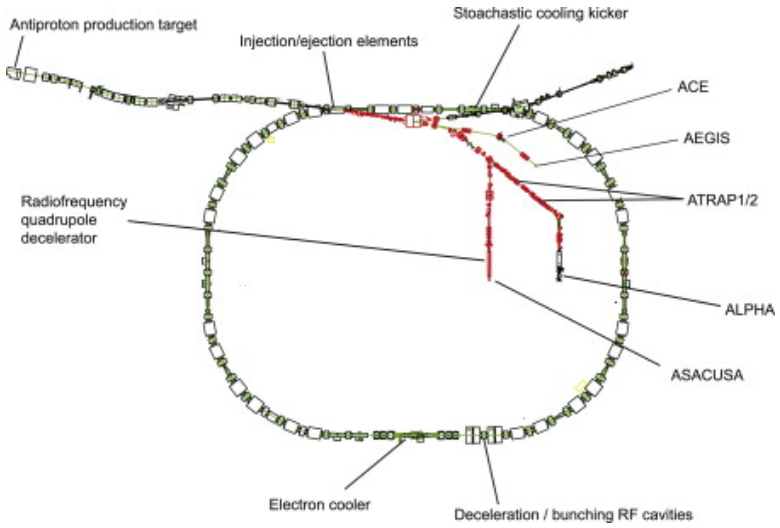

Figure 2.2: Overview of the AD hall with the experimental area (image from [14])

2.2 ASACUSA beamline

The setup of ASACUSA offers a few advantages for systematic antiproton annihilation studies. After injection into the ASACUSA beamline (Fig. 2.3), the antiprotons from the AD are first further decelerated by the RFQD (Radio Frequency Quadrupole Decelerator, see [15]) to energies of 115 keV. Then, after passing two degrader foils, the antiprotons are captured in the MUSASHI (Monoenergetic Ultra

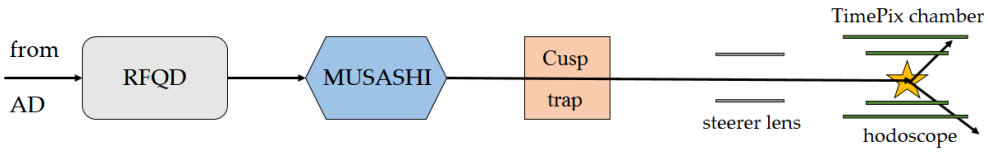

Figure 2.3: A schematic overview of the ASACUSA beamline

Slow Antiproton Source for High-precision Investigations, see [16]) trap, a Penning trap consisting of several ring electrodes aligned on the axis of a superconducting solenoid. A potential well keeps the antiprotons inside MUSASHI, where they are cooled via an electron plasma.
After cooling in the MUSASHI, the antiprotons are slowly extracted at an energy of 150 eV. They are extracted toward the Cusp trap (see [17]). If the ASACUSA setup is used for antihydrogen studies, the Cusp trap is where the mixing with positrons and thus production of antihydrogen happens. Originally, it was planned for the present experiment to operate right after MUSASHI, but it was unclear if the excellent vacuum conditions required in MUSASHI could be maintained in such a configuration. Therefore, the Cusp trap is kept in place and is followed by a CF100 four-way cross housing the Steerer lens (See Sec. 2.3) and a vacuum pipe which connects to the Timepix chamber. The chamber contains the target foil, where the antiprotons annihilate, and behind the Timepix3 detector (see Sec. 2.4) which detects the annihilation products. Timepix3 replaces the bismuth germanate (BGO) detector from earlier experiments during annihilation studies, providing improved resolution. The Timepix chamber is itself surrounded by the hodoscope (see Sec. 2.5). This combination of detectors allows for tracking and identifying the various annihilation products as well as covering a large solid angle.

2.3 Steerer Lens

As mentioned in Sec. 1.1, the beam was known to be off-center from earlier antiproton experiments. At small extraction energies this can be caused by a slight misalignment of the Cusp trap or by the Earth's magnetic field. However, in contrast to neutral antihydrogen, charged antiprotons are relatively easy to manipulate via magnetic or electric fields. So, in order to steer and focus the beam, a new device was introduced to the beamline, in front of the hodoscope and the Timepix chamber: the Steerer lens.
This Steerer lens is an electrostatic lens, basically a more elaborate version of an Einzel lens, with 5 electrodes and inclined cuts (see also Fig. 2.4), allowing for focusing as well as steering.
A classical Einzel lens consists of three cylindrical electrodes. In this version the

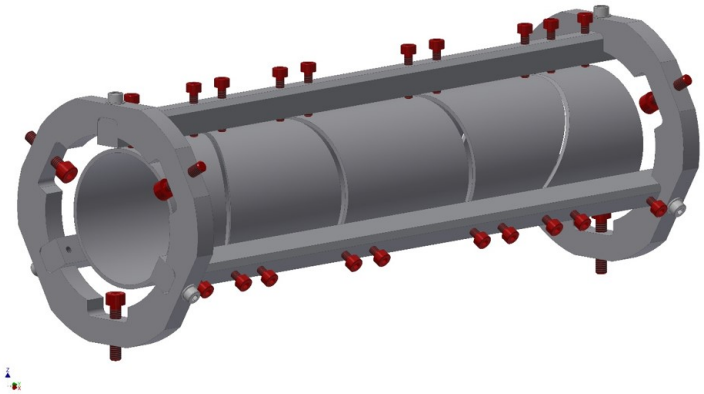

Figure 2.4: A 3D drawing of the Steerer lens. The 5 electrodes are held in place in the frame by isolating PEEK screws. The screws on the round end-pieces hold the steerer lens in place in the beam pipe. (image property of SMI)

entrance and exit electrodes are separated by a diagonal cut. This results in five electrodes and allows for steering perpendicularly to the beam axis. Ultimately, the energy of the beam is not changed by this. Simulations have been performed (see Sec. 3.2) to verify the working principle and geometric design. Then, the lens was produced in the SMI workshop. The mounting structure has to guarantee electrical insulation and well-aligned positioning of the five electrodes within the given space constraints.

After construction, assembly had to be tested and all parts had to be prepared for their usage in UHV. The parts were cleaned thoroughly at SMI and shipped to CERN for installation in the beam pipe.

Assembly of the Steerer lens

Assembly of the Steerer lens begins by building the mounting frame. Three bars, marked “1”, “2” and “3” respectively, have to be aligned with the same markings on the round end-piece labeled “A” on the side. Next, the other round end-piece, labeled “E” has to be attached. The labels “A” and “E” on the end-pieces have to be aligned. See also Fig. 2.5.

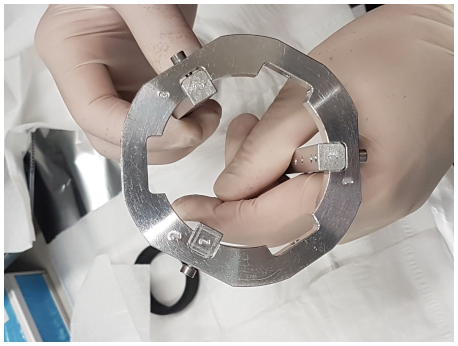

(a) Aligning the bars with the markings “1”, “2” and “3”.

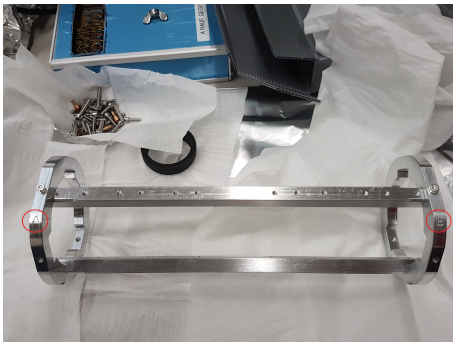

(b) Attaching end-piece “E”. Note how the markings “A” and “E” are aligned.

Figure 2.5: Assembling the frame of the Steerer lens.

Following this, the electrodes have to be assembled. They also have markings, from “A” to “E”, as well as holes for screwing them onto a holding bar and later wiring them. The markings and holes have to be aligned for screwing them onto the holding bar, which also has markings “A” to “E”. These have to match the markings on the electrodes, “A” to “A”, “B” to “B” and so on. The electrodes should be loosely screwed onto the small bar. They should stay in place, but still be able to move slightly. Fig. 2.6 shows the alignments mentioned.

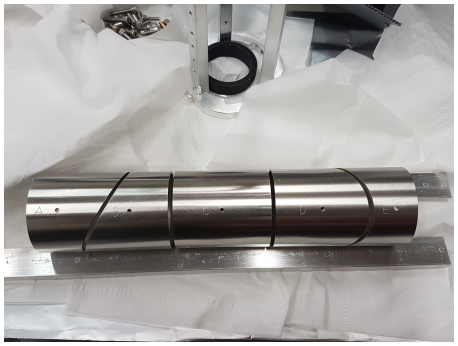

(a) Aligning the electrodes. “A” to “E” should be readable from left to right.

(b) A small bar keeps the electrodes in place.

Figure 2.6: Assembling the electrodes of the Steerer lens.

The next step is inserting the electrodes into the frame. To make sure that the electrodes sit at the right position inside the mounting frame, a distance ring (black PLA) was 3D printed to facilitate this step. The outer frame has to be propped

up and the black ring is placed in the center of the end-piece. Then the electrodes are inserted, until they rest on the ring. If end-piece “E” rests on the bottom, then electrode “E” should rest on the ring, otherwise it should be electrode “A”. This step is symmetric with respect to the position of the electrodes inside the mounting frame. When completely inserted, the electrodes have to be rotated until the labels on the bar align with those on the end-pieces of the frame. Fig. 2.7 shows these steps.

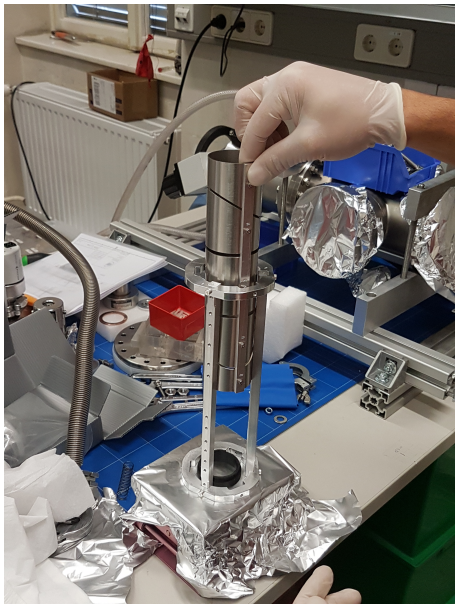

(a) The frame is propped up and the black distance ring placed in the center.

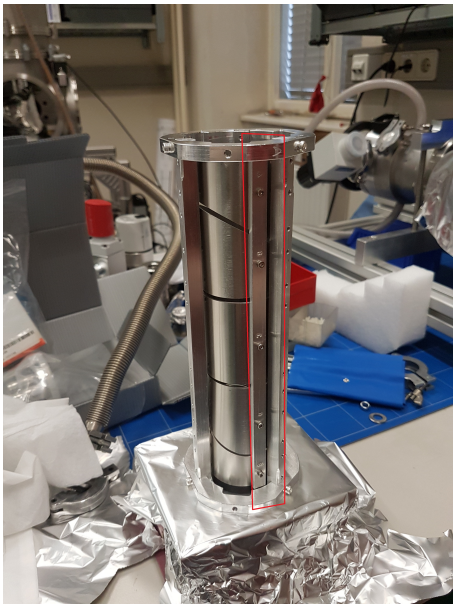

(b) The markings on the end-pieces and the electrodes have to be aligned.

Figure 2.7: The electrodes are inserted into the frame.

Now, the electrodes have to be fixed in place, in such a way that they are centered. To facilitate this step, three broad metal bars are first inserted into the frame, to further help keep the electrodes in place. Using a 2 mm L-shaped distance piece, the broad bars are inserted into the frame and screwed onto the end-pieces, using M4 slot-vented silver-plated socket-head screws. The electrodes should be as centered as possible before they are fixed in place by putting non-conducting PEEK screws through the screwholes in the three bars of the frame which connect to the ring-shaped end-pieces. The screws should press onto the electrodes evenly from all sides, without excessive force. See also Fig. 2.8.
The broad bars are removed again and the screws that held them in place are turned around. These keep the lens in place inside the vacuum chamber, so the frame will not be on a floating potential. The small labeled bar that keeps the

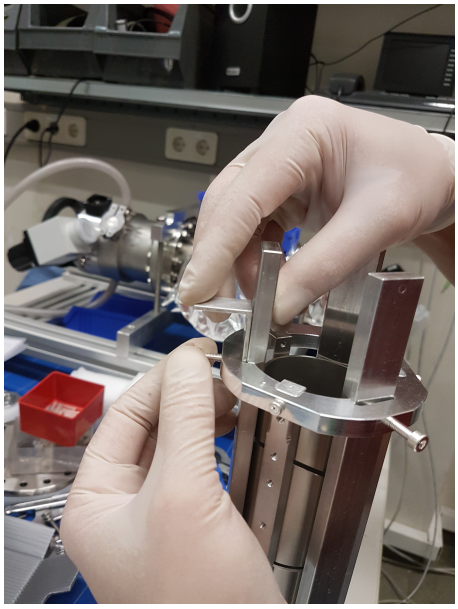

(a) The broad bars are inserted and positioned, using the L-shaped piece for coarse distancing.

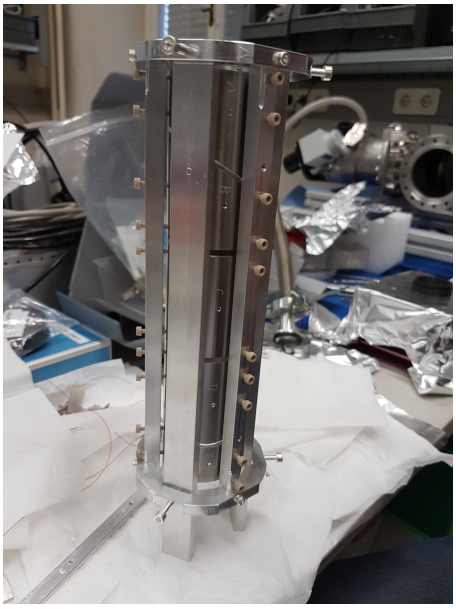

(b) PEEK screws hold the electrodes in place.

Figure 2.8: The electrodes are fixed onto the frame.

electrodes together is also removed since the screwholes beneath it are used for wiring the electrodes. The Steerer lens comes with 5 wires. One of them has loops on both ends, this wire connects electrodes "A" and "E", as they will share the same potential. The longest wire is attached to electrode "A", the shortest one to "C". The remaining wires should be of approximately the same length and are used for wiring electrodes "B" and "D" respectively. When attaching the wires with screws, special attention has to be paid not to screw the screws in too far - their tips should not reach inside the electrodes, since this could distort the electrical fields inside (see Fig. 2.9).

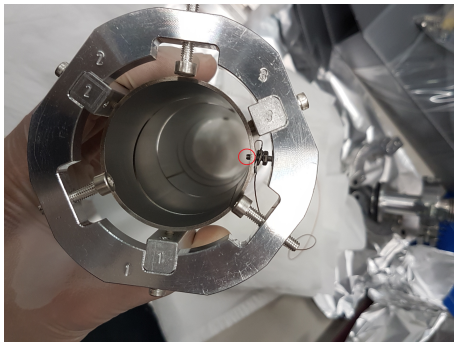

(a) A badly attached wire. The screw peeks inside the lens (circled red).

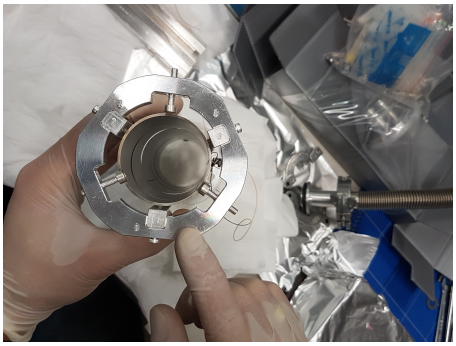

(b) Here the wire is attached correctly.

Figure 2.9: The electrodes are wired.

Finally, the lens is inserted into the vacuum chamber (see Fig. 2.10). The wiring is guided through an electrical vacuum feedthrough and the connections outside labeled accordingly.

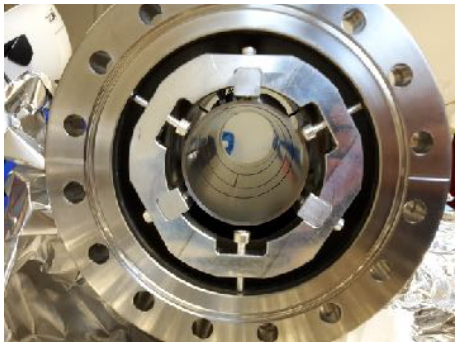

(a) The Steerer lens inserted into the vacuum chamber.

(b) Labels for the wiring.

Figure 2.10: Final steps of the assembly.

The Steerer lens at CERN

At CERN, the Steerer lens was inserted into a CF100 four-way cross right after the Cusp trap, in front of the TimePix chamber (see Fig. 2.14 for an overview of this part of the beamline up to the TimePix chamber). It was inserted such that bar "3" was on top, electrode "A" was positioned upstream and thus "E" downstream. Then, one shift of the beam time was used to find the optimal potentials for the electrodes to focus and steer the beam on center, using the BGO. Table 2.1 shows

the final potentials that were used. As one can see in Figure 2.11, the steering worked very well. As for the focus, a FWHM of 25 mm was achieved, which still leaves room for improvement. It is possible that the magnetic field generated by the Cusp trap, which was not included in the simulations, worked against better focusing. Therefore, measurements of the magnetic field around the hodoscope were conducted (see 3.3), in order to take this field into account in future simulations.

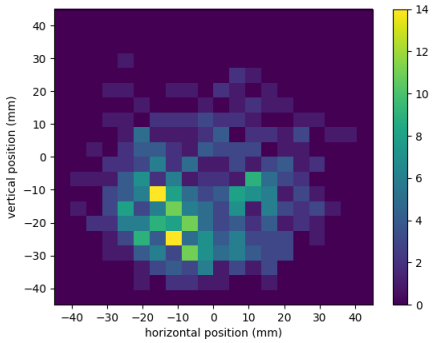

(a) The antiproton distribution on the BGO detector without usage of the Steerer Lens.

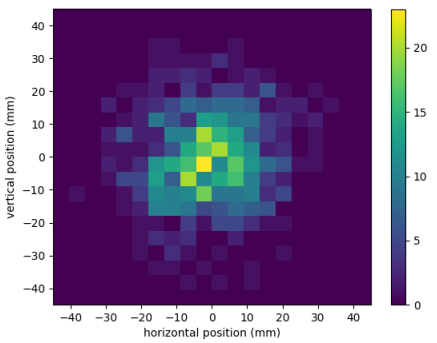

(b) The antiproton distribution on the BGO detector with the optimized potentials.

Figure 2.11: Comparison of the antiproton distribution on the BGO detector before and after finding the best potentials for the Steerer lens (images by B. Kolbinger).

$\mathbf{U}_{\mathrm{AE}}$	$\mathbf{U}_{\mathrm{B}}$	$\mathbf{U}_{\mathrm{C}}$	$\mathbf{U}_{\mathrm{D}}$
40 V	83 V	170 V	61 V

Table 2.1: The optimal values for the electrodes.

2.4 Timepix3 detector

During annihilation studies, the Timepix3 detector replaces the BGO inside the hodoscope. Timepix3 is a hybrid pixel detector. HPDs were originally developed as successor to silicon strip detectors, to circumvent problems that arise in High Energy Physics when tracking a large amount of particles in short times. One of these problems is an uncertainty called “ghost hits” when hit by several particles at the same time, as it is ambiguous which pairs of strips correspond to which hit.

Pixel detectors do not have this problem. Their sensitive area is pixelated, with each pixel having its own electronics. The contact between pixel sensor and electronics is achieved via bump-bonding (see Fig. 2.12) [18].

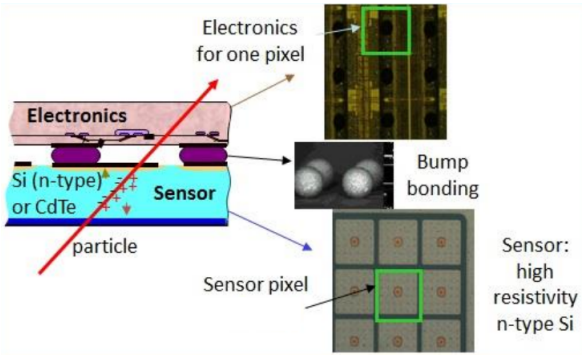

Figure 2.12: A schematic drawing of the structure of a hybrid pixel detector (image from [18]).

Timepix3 is a successor to the Timepix [19], and developed by the Medipix3 collaboration at CERN.
The detector chip consists of 256×256 pixels, with 55 µm pitch. Timepix3 allows for simultaneous measurements of time-over-threshold (ToT) and time-of-arrival (ToA) for every individual pixel. A 40 MHz coarse clock and a 640 MHz clock for fine measurements enable a time resolution of 1.6 ns. The readout logic allows for continuous data acquisition [20].

For ASACUSA, a quad array of 2×2 chips was used. This gives an active area of 28×28 mm^2. The readout-system SPIDR (Speedy PIxel Detector Readout, see [21]) was developed by NIKHEF. A bias voltage of 150 V was applied to deplete the sensor.
The Timepix3 quad array is placed inside the Timepix chamber (see Fig. 2.13), which also houses the carbon foil serving as a target for the beam. The foil has an area of 20×20 mm^2 and is 2 µm thick. It is placed on a holder ~1 cm away from the Timepix array, and also acts as a separator between the UHV in the Cusp ($\sim 10^{-10}$ mbar) and the vacuum in the Timepix chamber ($\sim 10^{-7}$ mbar). A voltage of 500 V to 1000 V is applied to the foil to further focus the antiproton beam and to avoid preferred annihilation on the surface which might suffer from impurities. The detector-array itself is mounted on its own aluminium support, which is also used for heat dumping. Some copper braids guide the heat to the back flange (see also 3.1 for the test of the cooling system). The flange also supports the readout system, and via a DN25KF in this flange, the chamber is evacuated. The chamber itself is surrounded by the hodoscope, such that the Timepix3 array is centered with respect

to the scintillating bars of the hodoscope.

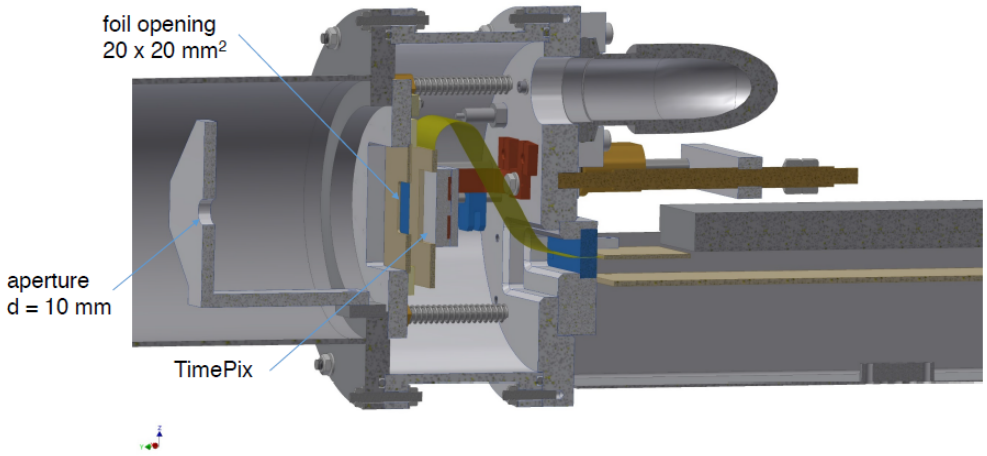

(a) A 3D drawing of the Timepix chamber. The aperture ($d = 10\,\text{mm}$) is optional and was not in place during measurements.

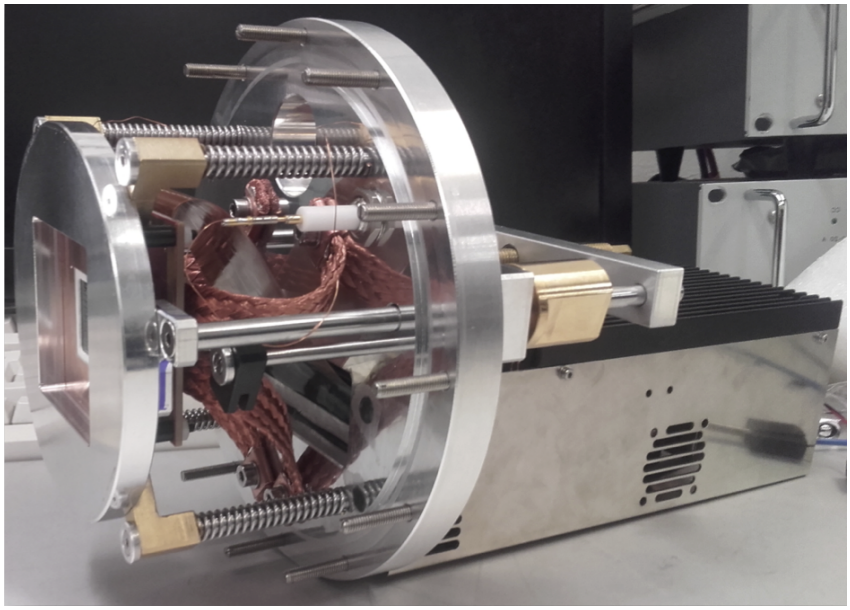

(b) A photo of foil, Timepix3 and readout.

Figure 2.13: The Timepix chamber (images property of SMI)

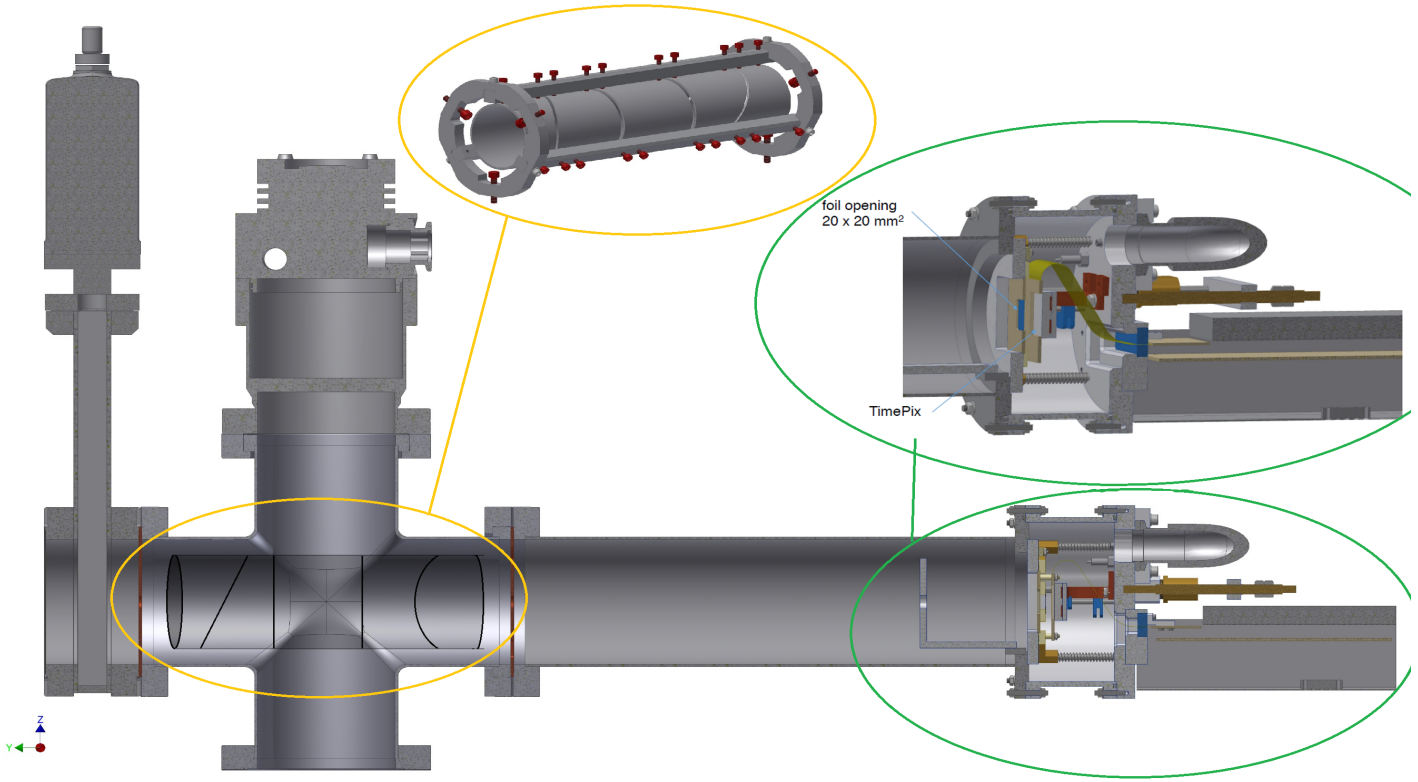

Figure 2.14: A 3D image showing the beamline from the four-way-cross to the Timepix chamber. The cross houses the Steerer lens as shown. The more detailed rendering of the Timepix chamber can also be seen in Fig.2.13 (image property of SMI)

2.5 Hodoscope

Hardware

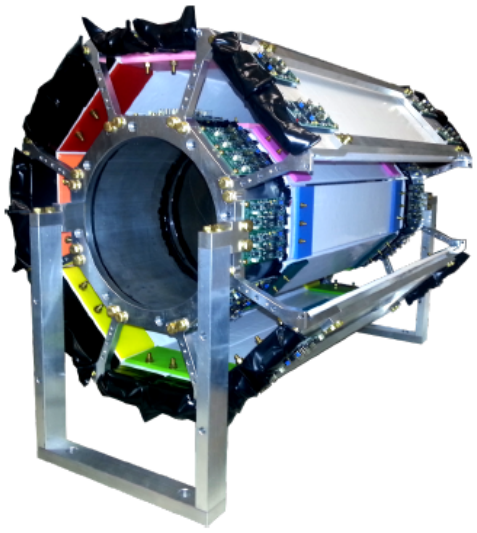

(a) An image of the hodoscope without the wiring. An outer panel has been removed for a better view of the inner layer. The colored braces are visible.

(b) A view of an outer hodoscope segment. The scintillating bars are wrapped in aluminum foil separately before being grouped up and wrapped in light blocking foil.

Figure 2.15: Images showing the hodoscope and one of its outer segments (images taken from [22])

The hodoscope consists of two layers made of fast response scintillator bars, the scintillating material is Eljen Technologies EJ-200. Each layer consists of 32 such bars. The inner layer is 180 mm in diameter. The scintillator bars used are 300 mm and have a cross section of $20 \times 5\,\mathrm{mm}^2$. This is reduced to $8 \times 5\,\mathrm{mm}^2$ by the light guides with a length of 40 mm on each side of the bar. The diameter of the outer layer is 345 mm. The scintillator bars are 450 mm long and have a cross section of $35 \times 5\,\mathrm{mm}^2$. The light guides with length 75 mm reduce this again to $8 \times 5\,\mathrm{mm}^2$. The scintillating bars are wrapped in aluminium foil individually and grouped into segments - 4 bars per inner segment, two for each outer one. The segments are wrapped in light blocking foil (see Fig. 2.15b). The scintillating light is detected by two Silicon Photo Multipliers (SiPMs) of type KETEK PM3350TS glued to both ends of each bar. This not only suppresses dark noise by requiring a coincidence

between both sides, but also allows for a coarse determination of the hit position by taking the timing difference between both sides and their respective pulse heights into account.
The segments are attached to an aluminium frame. This material is of low density ($\rho = 2.70\,\mathrm{g\,cm^{-3}}$) and has a large radiation length, reducing the probability of pions from $\overline{\mathrm{p}}$ annihilations interacting and scattering with it. The frame is a pipe of 1 mm thickness with arms for the outer layer. They form an octagonal barrel, covering a solid angle of ~73 %, assuming annihilations take place exactly in the center. Each segment is attached via a colored plastic brace, which allows for labeling the parts. The colour of the read out channel wires is the same as its corresponding segment (green wire for the green segment etc). This facilitates wiring and detecting any errors. Fig. 2.15a shows the hodoscope assembled.
This whole structure is mounted on a movable cart made of aluminium profiles. Moving the detector is very easy, and reproducibility of the in-beam position is ensured with metal plates that can be screwed to the profiles.

A more in-depth description of the hodoscope's hardware, its assembly and testing can be found in the master thesis of A. Capon [22].

Electronics

The hodoscope is read out via so-called IFES-boards (Intelligent Front-End Electronics for Silicon-Photomultipliers, see Fig. 2.17). These were designed in the scope of C. Sauerzopf's dissertation [23], so a detailed description can be found there. This part shall only cover the necessary components for understanding their functionality.

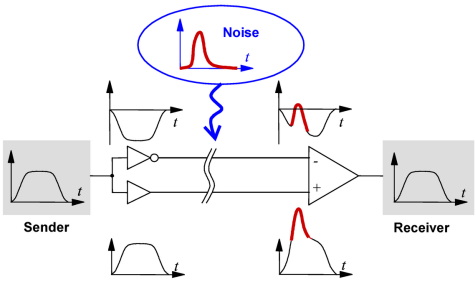

Figure 2.16: A schematic overview of differential signaling. (source: `http://commons.wikimedia.org/w/index.php?curid=18321195`)

To be able to operate the modules in harsh environments like accelerator facilities, it is extremely important to transport the signal without distortion or noise pick-up. These boards use differential signaling to achieve this. The original signal is split up

into two and run through twisted cabling, with one of the two signals inverted. Both pick up the same amount of noise, which is canceled out by the receiver subtracting them, so only the pure, original signal remains (see Fig. 2.16). All signals on the board are differential. Additionally, for the control bus and the digital output, LVDS (Low Voltage Digital Signal) drivers are used. These ensure a standardized stable and low-noise signal even for long paths.

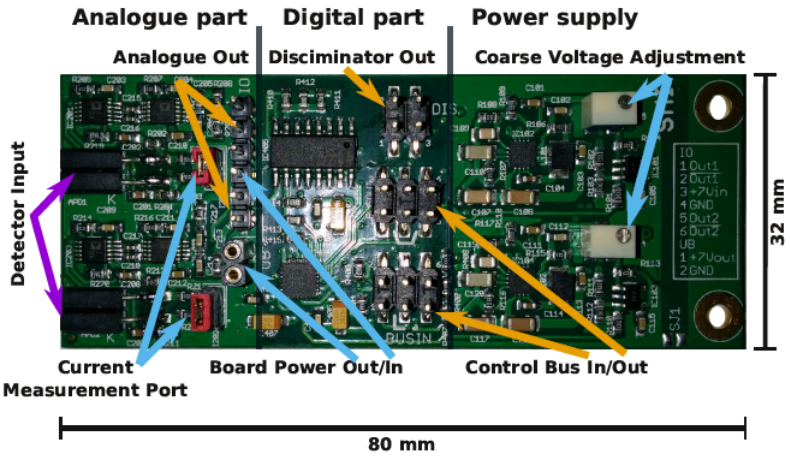

Figure 2.17: A photo of an IFES module (image taken from [23]).

Coarse amplification gain can be set via an on-board potentiometer. The fine gain, as well as the threshold to generate Time-over-Threshold (ToT) signals, can be set remotely via an Arduino microcontroller connected to the IFES boards via an SPI bus.
First, the signal coming from the detector is received by a broad band amplifier. The amplified analogue signal is fed to the leading edge discriminator. The starting time of the discriminator's pulse is determined by the leading edge of the analogue signal and the set threshold. The length of the pulse is determined by the length of the analogue signal as long as it is above threshold, producing a ToT signal. Both the analogue amplified signal and the ToT are provided to the user.

Fiber Upgrade

In 2017, the hodoscope received an upgrade. To improve position resolution along the beam axis, 2 layers of scintillating fibers (Saint Gobain BCF-12) were added. These layers are made of square scintillating fibers ($2 \times 2\,\mathrm{mm}^2$), wound around the detector axis so the fibers run perpendicular to the scintillating bars of the hodoscope. Each channel consists of 4 such fibers bundled together, resulting in a total edge length of 4 mm per bundle. They are read out single-sided via a SiPM

(KETEK PM3350-EB).
The fibers are wound around a supporting carbon tube with a slight overlap, as the end without a SiPM is tucked under the end with one, reducing the stress on the end where the SiPM is glued to. The fiber bundles are held in place by supporting plastic rings. The outer fiber layer has 100 channels and a diameter of 292 mm, it sits between the two layers of scintillating bars. The inner fiber layer has 63 channels and a diameter of 167 mm, sitting inside the inner hodoscope layer. Its carbon tube replaces the supporting aluminium tube.

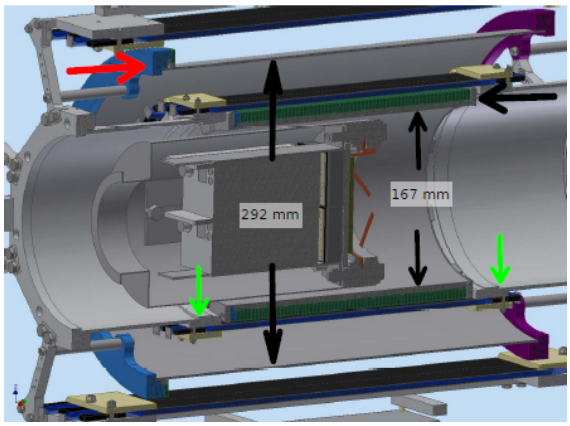

(a) A drawing showing the fiber upgrade. The red arrows point to the end-pieces of the outer fiber layer, black arrows mark the positions of the carbon tubes. Between the green arrows, the inner aluminium support is fully replaced by the inner fiber layer.

(b) The inner layer of the fiber upgrade, fully assembled.

Figure 2.18: Images showing a drawing of the fiber upgrade and the inner layer after assembly (images taken from [24]).

The read-out electronics for the upgrade work similarly to the IFES-boards described before.

The fiber upgrade was developed in the scope of M. Fleck's master thesis [24], so detailed information can be found there.

3. Simulations and Measurements

3.1 Cooling the Timepix3 detector

Under operation a power dissipation of about 2 W needs to be guaranteed for the Timepix3, which is a challenge in vacuum. Without a cooling mechanism the detector is expected to heat up to about 200 °C. A very simple cooling method was tested: a block of copper attached to the back of the detector, with flexible copper bands guiding the heat to a flange.
The testing setup looked as follows (see also Fig. 3.1): two copper braids are fixed between two aluminum blocks ($3 \times 3 \times 0.3\,\mathrm{cm}^3$ and $3 \times 3 \times 0.7\,\mathrm{cm}^3$ respectively), one of which has two indents just broad enough for the bands. The contact areas are covered in indium. The blocks were pressed together with a hydraulic press and subsequently screwed together so everything stays in place. Glued to this is a copper block ($4 \times 4 \times 1\,\mathrm{cm}^3$). The ends of the braids are covered in heat paste and screwed onto a blind flange. A heating resistor was used to simulate the heatload of the Timepix3, and a PT100 to measure the change in temperature. Both were covered in heat paste and screwed onto the copper block.
The setup was inserted into a small vacuum chamber, in such a way that it could hang freely, without contact to the walls. The wiring of the resistors is guided through an electrical vacuum feedthrough. The heating resistor is connected to a power supply, the PT100 to a voltmeter. The chamber is pumped via a second port, all other openings are covered with blind flanges.

First, a few short-time tests were conducted. The heating resistor was supplied a certain amount of power, and the resistance of the PT100 (and thus the temperature of the block, see also the appendix A) was measured after stabilizing. The results can be seen in Tab. 3.1
These short tests were followed by a long-time-test to see if the block would also provide stable long-time cooling for the duration of the experiment. The heating resistor was provided with 2.14 W, as expected from Timepix3 during the actual experiment. Over the course of one week, the testing setup was checked every day to see if there were any unexpected changes in the temperature of the copper block.

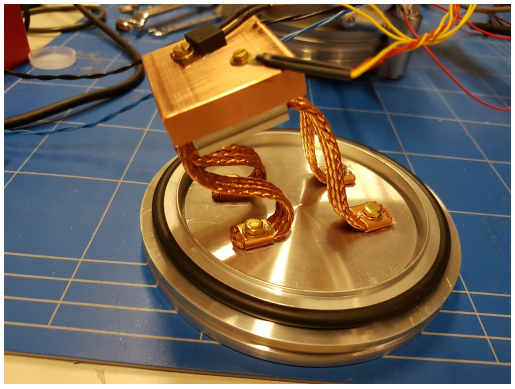

(a) The blocks are screwed onto a blind flange.

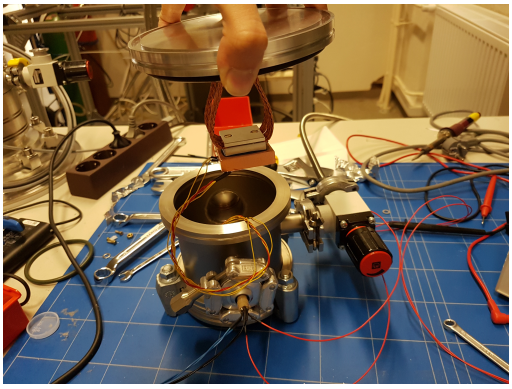

(b) The setup is inserted into the little chamber

Figure 3.1: The testing setup for cooling the Timepix3

P (W)	**U** (V)	**I** (A)	**R** (Ω)	**T** (°C)
1.09	5.000	0.218	111.75	29.38
2.14	7.000	0.306	114.80	37.00
3.15	8.500	0.371	117.31	43.28

Table 3.1: This table shows the power supplied to the heating resistor, the corresponding voltage and current, the resistance of the PT100 for stable condition and the corresponding temperature of the block of copper.

The recorded values can be seen in Tab. 3.2.

The short tests show that the block keeps the experiment below 45 °C, even at over 3 W. The long test showed an even lower temperature than the short test, which may have been caused by the lab's air conditioning. It was concluded that this setup, together with a fan cooling from the outside, would sufficiently cool the actual experiment.

Day	Time	R (Ω)	T (°C)
Monday	11:55	114.56	36.40
Tuesday	12:00	114.44	36.10
Wednesday	13:20	114.52	36.30
Thursday	11:44	114.40	36.00
Friday	11:15	114.36	35.90
Saturday	13:35	114.55	36.38

Table 3.2: The values for the resistance of the PT100 and the corresponding temperature of the copper block. The measurements took place between Monday, September 25, 2017 and Saturday, September 30, 2017.

3.2 COMSOL simulations of the Steerer lens

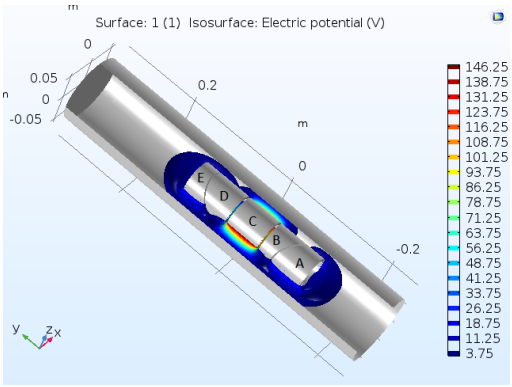

(a) A simulation of the electric field of the Steerer lens. A part of the surrounding pipe has been cut out.

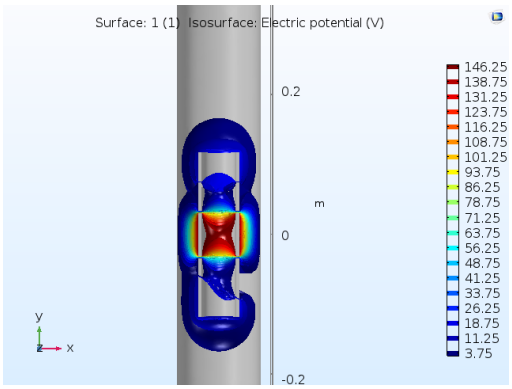

(b) The same field seen from above, with the electrodes of the lens cut open for a better view.

Figure 3.2: A possible electrical field of the Steerer lens. Here, electrodes A and E share a potential of 25 V, B and D are grounded, and C has a potential of 150 V

Before the production of the Steerer lens was issued, simulations in COMSOL[1] were performed to see if the lens would fulfill its purpose as intended.
To do so, at first the geometry of the lenses' electrodes was modeled, as was a surrounding vacuum pipe. The material of all components was chosen to be stainless steel, the surrounding areas were chosen to be air. The boundaries of all 5 single

[1] `http://www.comsol.de`

electrodes were defined as separate entities via the **Definitions** toolbar, this makes setting the boundary conditions and mesh much easier.
The outer electrodes (labeled "A" and "E") were set to a common potential, and a fine mesh was chosen for all electrodes. For each set of values for the potentials, the resulting electrical field was simulated using COMSOL's Electrostatics (es) module. One resulting field can be seen in Fig. 3.2.
Using these simulations of the electrical field, the resulting particle trajectories could be simulated too. In the **Add Physics** menu, the module Charged Particle Tracing (cpt) was added. One end of the surrounding pipe was defined to be the outlet of the simulated beam. After setting the charge and the energy to simulate 150 eV antiprotons, the particles were released from a grid. A looped animation (see Fig. 3.3) showed that the focusing would work very well. The steering was hardly visible for small potentials (as expected, since the particles would only be deflected by a very small angle). By setting the steering potentials very high, their effect could be seen very clearly.
It was concluded that the Steerer lens would work as intended.

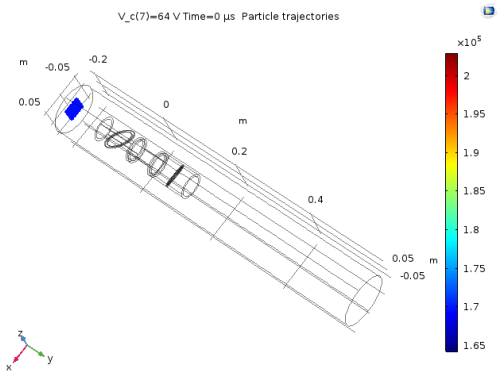

(a) A virtual pbar beam being released into the simulation.

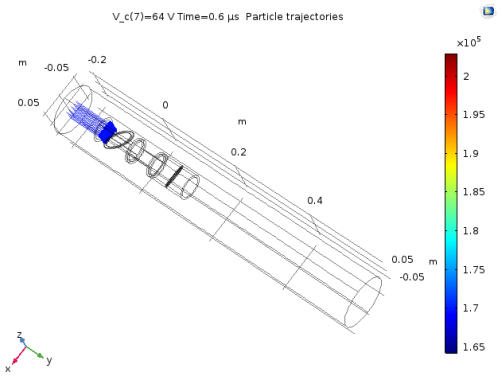

(b) The pbars enter the lens.

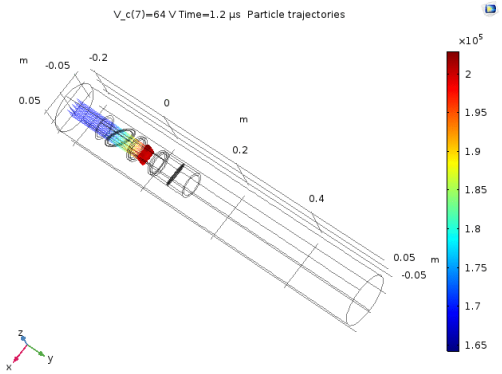

(c) The particles are focused by the central electrode.

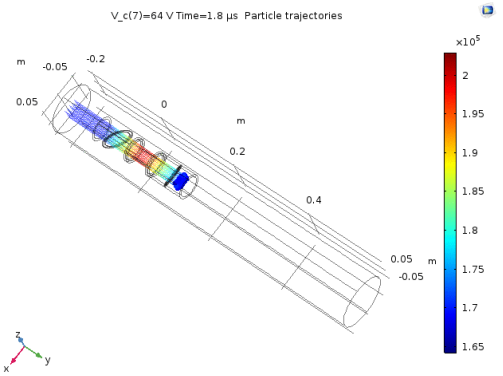

(d) The beam passes the last electrodes.

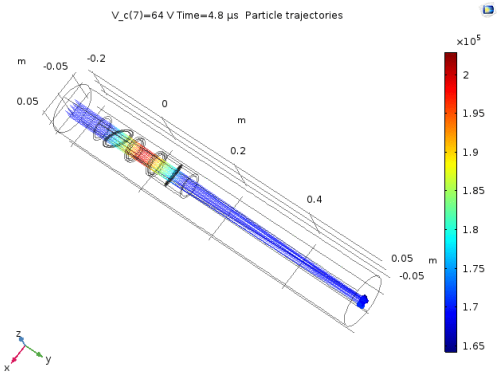

(e) The particles reached the end of the simulated vacuum pipe. One can clearly see that the beam has been focused.

Figure 3.3: A simulated pbar beam passing through the Steerer lens in several steps.

3.3 Magnetic Field around the hodoscope

At CERN it became obvious that while the steering with the Steerer lens worked as planned, the focusing effect was not as strong as expected (FWHM of 25 mm). It is possible that the magnetic field of the Cusp trap prevented better focusing. To check this and to include this field in future simulations, measurements were performed on-site. Using fluxgate sensors, the field was measured at several spots around the hodoscope, as was the distance of these spots from a fixed point of reference on the frame as the origin. The space coordinate system was chosen as follows: the z-axis is parallel to the direction of the antiproton beam, the y-axis goes from the ground upward, and x goes parallel to the ground, forming a right-handed coordinate system with the other two axes. The positive direction of the sensors was chosen to be in the same direction as the cables coming out of the metal casing.

Calculating the Offsets

To check the magmeter for a possible offset, some calibration measurements were performed in a magnetically less busy area, choosing a space-coordinate system again, rotating the device in all 24 possible orthogonal orientations in space and recording the three sensor values every time, leading to a total of 72 readings. The unsorted values can be found in the Appendix in Table B.1.

The values were first sorted into three groups, where each group contains only the 24 measurements done by one of the three sensors. These are then further divided into 3 subgroups of 8 values each, according to which of the three field component has been measured (see tables 3.3). The first four rows in these tables show the positive measurements, the last four the negative ones when the measuring sensor was flipped. For a perfect device, one would expect these values to be of the same magnitude, differing only in their sign. The sum over all the values would vanish. This obviously is not the case here. For each axis of the device and each component of the magnetic field, a "positive" (for the first 4 rows) and a "negative" (last 4 rows) mean was calculated, as was a corresponding standard deviation. These were combined into offset and standard deviation for each of them (see tables 3.4, 3.5 and 3.6).

$\mathbf{B_x}$ (µT)	$\mathbf{B_y}$ (µT)	$\mathbf{B_z}$ (µT)
41	10	29
33	24	26
37	6	24
36	15	29
−35	−18	−22
−34	−19	−19
−33	−5	−23
−34	−17	−35

(a) Measurements by the x-sensor.

$\mathbf{B_x}$ (µT)	$\mathbf{B_y}$ (µT)	$\mathbf{B_z}$ (µT)
38	11	26
29	18	26
34	5	23
37	22	30
−35	−12	−22
−32	−15	−21
−30	−4	−21
−36	−21	−22

(b) Measurements by the y-sensor.

$\mathbf{B_x}$ (µT)	$\mathbf{B_y}$ (µT)	$\mathbf{B_z}$ (µT)
39	18	28
40	11	27
37	−3	32
44	1	34
−28	−29	−17
−28	−28	−19
−27	−27	−21
−30	−26	−21

(c) Measurements by the z-sensor.

Table 3.3: B_x, B_y and B_z as measured by the different sensors of the magmeter during calibration measurements.

	$\mathbf{B_x}$ (µT)	$\mathbf{B_y}$ (µT)	$\mathbf{B_z}$ (µT)
mean pos	37	14	27
Stdev pos	3	8	2
mean neg	−34	−15	−25
Stdev neg	1	7	7
Offset	1	−1	1
Stdev Offset	2	5	4
Offset x-sensor		1	
Stdev		2	

Table 3.4: The calculated means, standard deviations and the resulting Offset for the x-sensor of the magmeter.

	$\mathbf{B_x}$ (µT)	$\mathbf{B_y}$ (µT)	$\mathbf{B_z}$ (µT)
mean pos	35	14	26
Stdev pos	4	8	3
mean neg	−33	−13	−22
Stdev neg	3	7	1
Offset	1	1	2
Stdev Offset	2	5	1
Offset y-sensor		2	
Stdev		1	

Table 3.5: The calculated means, standard deviations and the resulting Offset for the y-sensor of the magmeter.

	$\mathbf{B_x}$ (µT)	$\mathbf{B_y}$ (µT)	$\mathbf{B_z}$ (µT)
mean pos	40	7	30
Stdev pos	3	10	3
mean neg	−28	−27	−20
Stdev neg	1	1	2
Offset	6	−10	5
Stdev Offset	2	5	2
Offset z-sensor		5	
Stdev		2	

Table 3.6: The calculated means, standard deviations and the resulting weighted Offset for the z-sensor of the magmeter. Note the discrepancies between the overall means.

Using the standard deviations σ_i of the offsets, each offset was given a certain weight w_i (with i indicating the field component):

$$w_i = \frac{1}{\sigma_i^2}$$

A bigger Standard deviation means that the influence of the corresponding weighted offset $O_{weighted,i}$ gets small (μ_i is the offset resulting from combining the means):

$$O_{weighted,i} = \frac{1}{w_x + w_y + w_z} \cdot w_i \cdot \mu_i$$

The resulting final offset for each sensor is the sum of these weighted offsets:

$$O_{sensor} = \sum_{i=x,y,z} O_{weighted,i}$$

These calculated Offsets for the sensors were then subtracted accordingly from the values measured around the hodoscope.

Looking at the data and the results, it is obvious that one has to be careful with the interpretations. Especially the offsets for the z-sensor have large fluctuations.
There was a notable change of several µT in the values of the magnetic field when the device was even slightly tilted. This was especially a problem when the magmeter was turned on a side that had a cable coming out of it, making flat positioning on the surface difficult (see Fig. 3.4). It is possible that this was a source of these notable discrepancies. If these measurements are repeated, a better way has to be found to correctly position the magmeter so its positions are truly orthogonal.

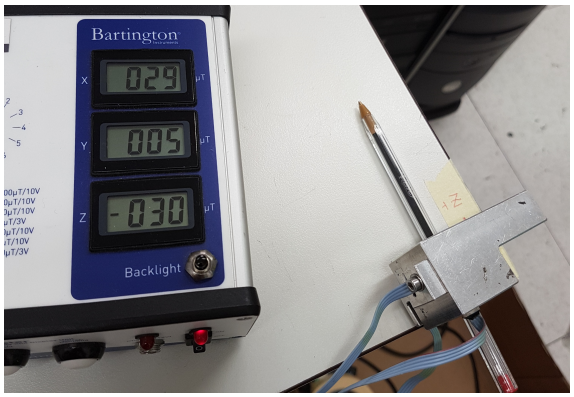

Figure 3.4: A photo taken during calibration measurements. The device is flipped on a side with a cable coming out of it. A pen was used to help placing it parallel to the desk's surface. It is possible that the device was still slightly tilted, distorting the measurement.

Fitting the field

For all further analysis, the origin of the space coordinates was shifted from the arbitrarily chosen point of reference to the center of the Cusp trap. After this, the first thing to note was that several values for either B_x, B_y or B_z were above 1000 µT (the recorded data adjusted for their offsets can be found in table B.2). These datapoints were discarded entirely, since those were out of range of the magmeter

used.
The remaining data was visualized using gnuplot[2]. Three 2D plots were produced, one for each plane of the coordinate system (XY, XZ and YZ respectively), showing the points in space and the magnetic field at these points as projections in these planes. These visualizations can be seen in Fig. 3.5, 3.6 and 3.7. As expected, a trend is visible. Next, a fit to a simple magnetic dipole field, according to Formula 3.1 was conducted.

$$\vec{B}(\vec{r}) = \frac{\mu_0}{4\pi|\vec{r}|^2}\frac{3\vec{r}(\vec{m}\cdot\vec{r}) - \vec{m}|\vec{r}|^2}{|\vec{r}|^3} \tag{3.1}$$

With μ_0 (vacuum permeability, $4\pi \cdot 10^{-7}\,\mathrm{N\,A^{-2}}$), $\vec{r}$ (the distance from the dipole's origin, here the distances x, y and z from the center of the Cusp) and the three components B_x, B_y and B_z known, the components of the magnetic moment $\vec{m}$ had to be found. First, the three equations were fit independent of each other using gnuplot, but the results spanned several orders of magnitude.

The equations had to be fit simultaneously. To do so, a python script, using the symfit package[3] was written. The order of magnitude gnuplot calculated most often was used as the initial guess for this fit, but the field resulting from this fit did not match the measurements well at all. Adjusting the formula a little (changing the order of magnitude of μ_0 to be 10^5 instead of 10^{-7} to change the stop criterion), changing the initial guesses (especially lowering the order of magnitude for the initial values for m_x and m_y, as the main contribution is to be expected from m_z), and accounting for these changes in the final result, a more accurate fit could be found. The final python script for these fits can be found in Appendix C.
With this, the three components of the magnetic moment $\vec{m}$ were determined to be as in Tab. 3.7.

Parameter	Value ($\mathrm{kA\,m^2}$)	Standard Deviation ($\mathrm{kA\,m^2}$)
m_x	-7.2	1.3
m_y	-0.1	1.1
m_z	-23.8	0.7

Table 3.7: The calculated values of the components of the magnetic moment.

Finally, the results of the fit were compared with the measurements. The magnetic field caused by the magnetic moment received via the fit was calculated and the

[2] `www.gnuplot.info`
[3] `http://symfit.readthedocs.io/en/stable/intro.html`

resulting field was plotted into the visualizations in Figs. 3.5, 3.6 and 3.7. The field resulting from the fit seems to be in reasonable agreement with the measurements.

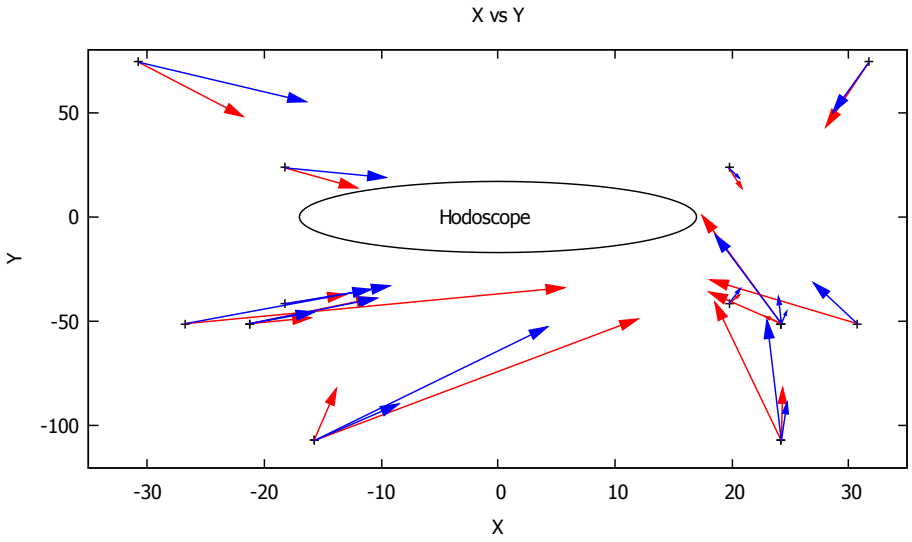

Figure 3.5: The projection of the measured (red) and the modeled (blue) magnetic field in the X-Y-plane (upstream view). An ellipsis for the hodoscope was added for better orientation (not to scale, the hodoscope appears elliptical because of the axis scale). 1 unit on either axis equals 1 cm for distance and 10 µT for the magnetic field.

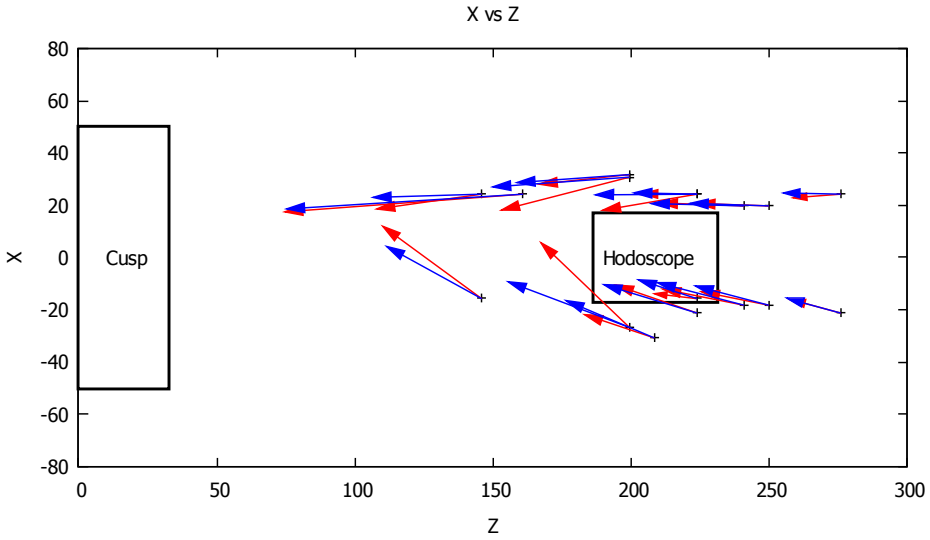

Figure 3.6: The projections in the X-Z-plane - this equals a bird's eye view of the setup. Hodoscope and Cusp are not to scale. Color coding and axis scales are the same as before.

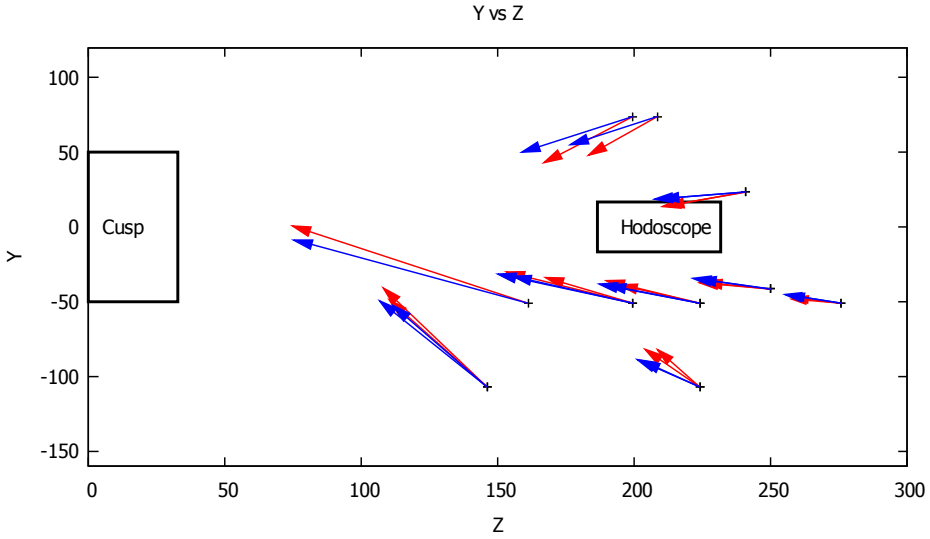

Figure 3.7: The Y- and Z-components of the magnetic field - a view of the setup from the side. Hodoscope and Cusp not to scale. Color coding and axis scales are the same as before.

3.4 Timepix3 data

During the beamtime in December 2017 at ASACUSA, 4 shifts were used for measuring $\overline{\mathrm{p}}$ annihilations on carbon with the Timepix3. About 380 runs were recorded, each showing about 240 antiproton events, resulting in roughly 90 000 events overall. The analysis of this data was done in ROOT[4].

How data were taken

As already mentioned in Sec. 2.2, the basic idea is the following: The antiprotons trapped and cooled in MUSASHI are slowly extracted at 150 eV. They are guided through the Cusp trap before being focused and steered onto the carbon foil by the Steerer lens. The antiprotons annihilate with either a proton or a neutron of the carbon atoms, and the resulting fragments (both HIPs and MIPs) hit the Timepix3 and/or the hodoscope.

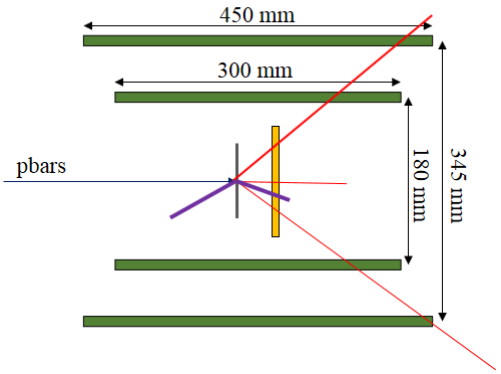

Figure 3.8: A typical annihilation event. The pbars hit the carbon foil (grey), annihilating into MIPs (red lines) and HIPs (purple). Whenever the hodoscope registered simultaneous pion hits in the inner and outer layer (one of the red lines crossing the green layers), the event was time-stamped in the Timepix3 data stream.

Both detectors were synchronized via a common Run Control, starting them simultaneously for each run. Every time the hodoscope registered an event (a pion coincidence, see Fig. 3.8), a trigger was issued to the SPIDR R/O and a time-stamp added to the event in the continuous Timepix3 data stream. One run lasted for about 70 s, with the extraction of the antiprotons happening within 20 s (see Fig.3.9).

[4] `http://root.cern.ch/`

The data taken by each of the 4 Timepix3 chips was originally saved in binary format as .dat files. They were first converted into .root files. As the name suggests, these are a special type of file for CERN's ROOT framework and aim to optimize compression of and access to large amounts of data. These files store data in so-called "trees". One such "tree" can have multiple "branches". The variables measured in the experiment form the "leaves" on each "branch".
The ROOT-files obtained from the Timepix3 chips contained 2 trees, `rawtree` and `timetree`. The timestamps were saved in the `timetree`, in a branch called `TrigTimeGlobal`. The branches of `rawtree` contained the information of the hits gathered by the Timepix3:

- `Row` contains the number of the row of the hit pixel
- `Col` contains the number of the column of the hit pixel
- `ToT` contains the Time over Threshold of the hit pixel
- `ToA` contains the Time of Arrival of the hit pixel
- `Track` counts the number of clusters (if several neighboring pixels are hit at the same time, this counts as a cluster)
- `NHits` gives the number of pixels for each cluster
- `GlobalTime` records the time, its counter was started via the common Run control for each run, synchronizing Timepix3 and the Hodoscope

`GlobalTime` and `TrigTimeGlobal` were saved as unsigned 64-bit longs, the rest were integer variables.

A glimpse at the data

A first look at the data shows a very clean signal with no background. Both HIPs and MIPs can be observed for most events. HIPs can easily be distinguished from MIP signals. Heavy fragments are surrounded by a "halo" in the Timepix data, as they induce a signal in their neighboring pixels proportional to their overall charge. Another effect that heavy charged particles show is a wider track compared to MIPs. This may be a so-called plasma effect, where the large local charge deposit effectively shields the inner region from the bias electric field, so the charge spreads laterally.

Since Timepix3 takes data continuously, all hits registered during one run can be plotted into one hitmap, resulting in a very busy picture (see Fig. 3.11a). It is important to first isolate single events. To do so, the time stamps in the datastream were used.

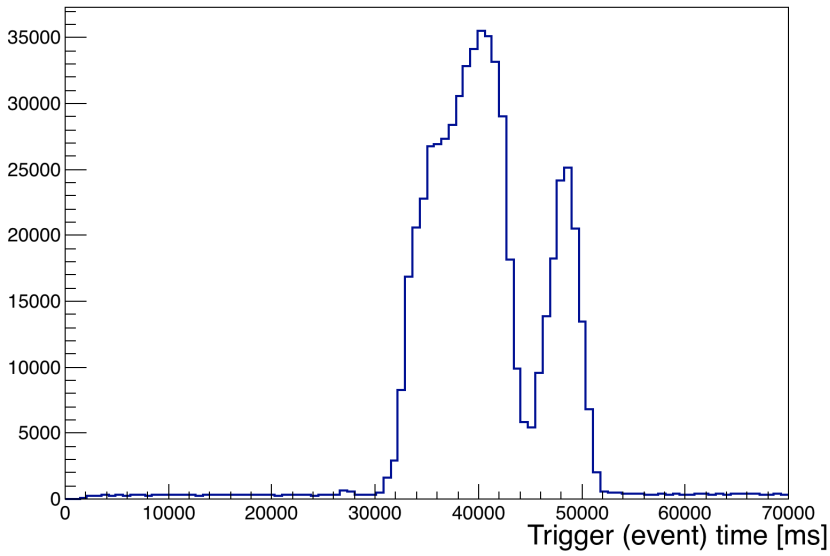

Figure 3.9: The typical time-distribution of hits during one run. The two peaks result from the way the antiprotons are cooled before extraction. (image by A. Gligorova)

The time-stamps were set whenever the aforementioned trigger condition for the hodoscope was satisfied, which of course happens after the particles in question have already passed Timepix3. It is thus necessary to "look back in time" to find the pions in the Timepix3 data, but also "into the future" to see the heavier (and thus slower) fragments. The goal is to find an appropriate (symmetrical) window around the time-stamp, long enough to see the relevant events, but not so long as to include unrelated ones.
Using a program, the optimal window of time was determined. The program combines the data of all 4 chips, produces a "clear" hitmap (see Fig. 3.11b) around the time-stamps for a given time-window for the whole Timepix3 array, and it is able to recognize separate clusters. The time-window was varied, and for each value a text file produced, showing the number of each analyzed run, the total number of clusters recorded for this run, and how many time-stamps had 1, 2, 3, 4, 5 or more than 5 clusters.
The time between an event in the Timepix3 and the resulting time-stamp was thus determined to be about $\pm 0.425\,\mu s$, the lowest window to see everything in the resulting hitmaps. For lower values, the chance to miss related hits is rising. Fig. 3.10 shows the distribution of hits for several time-windows. The window used for further analysis had to be chosen in an area where very little of this distribution changed. One can see that from $\pm 0.425\,\mu s$ onward, the distribution stays constant for a long span of time before increasing significantly at $\pm 500\,\mu s$. From this, the

window to conduct further analysis was determined to be ±1 µs.

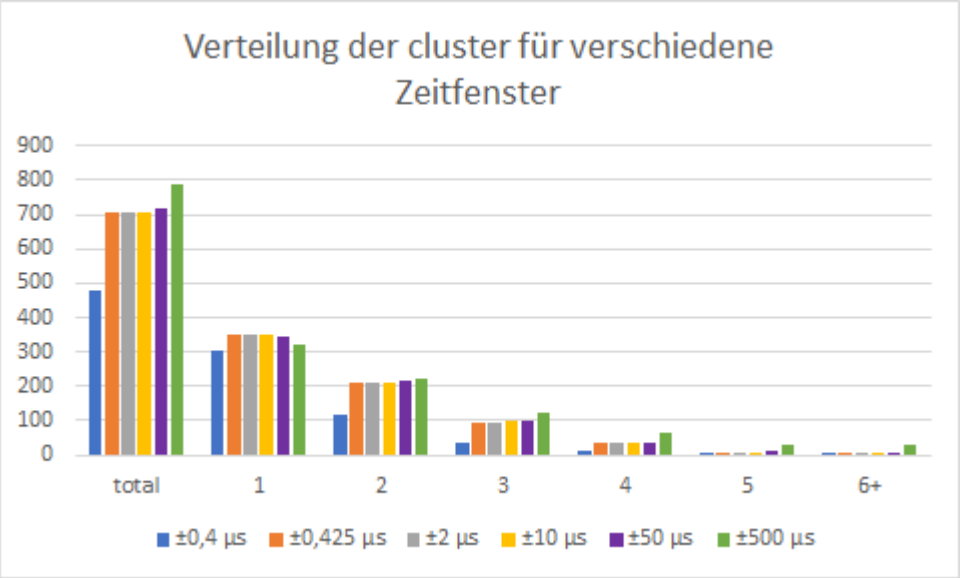

Figure 3.10: A bar diagram showing the distribution of the clusters for several time-windows. The leftmost set of bars indicates the (mean) total number of clusters for each time-window, followed by the number of hitmaps showing 1, 2, 3, 4, 5 or more than 5 clusters. One can see that ±0.4 µs is too small, as about a third of the events is missing. From ±0.425 µs onward, the distribution stays constant for a long span. Time windows that are too high obviously shift the distribution of clusters toward higher numbers, indicating that either "past" or "future" events are wrongly assigned to the timestamp in question.

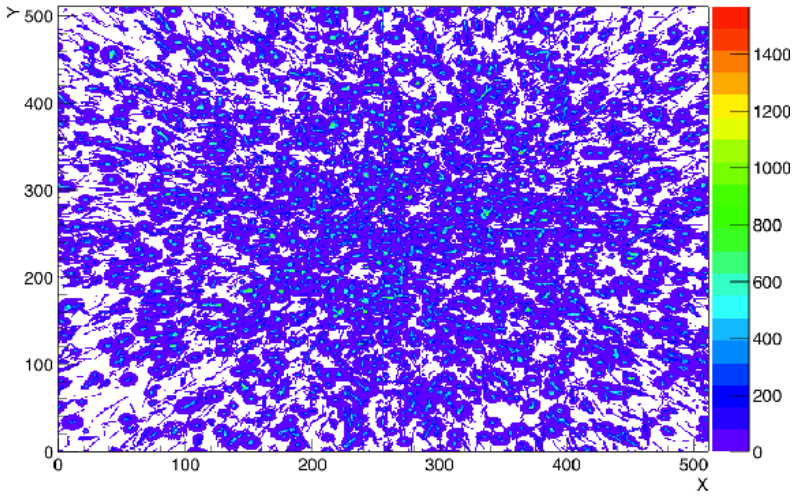

(a) A hitmap showing all hits registered during one run. The units on the energy scale are arbitrary

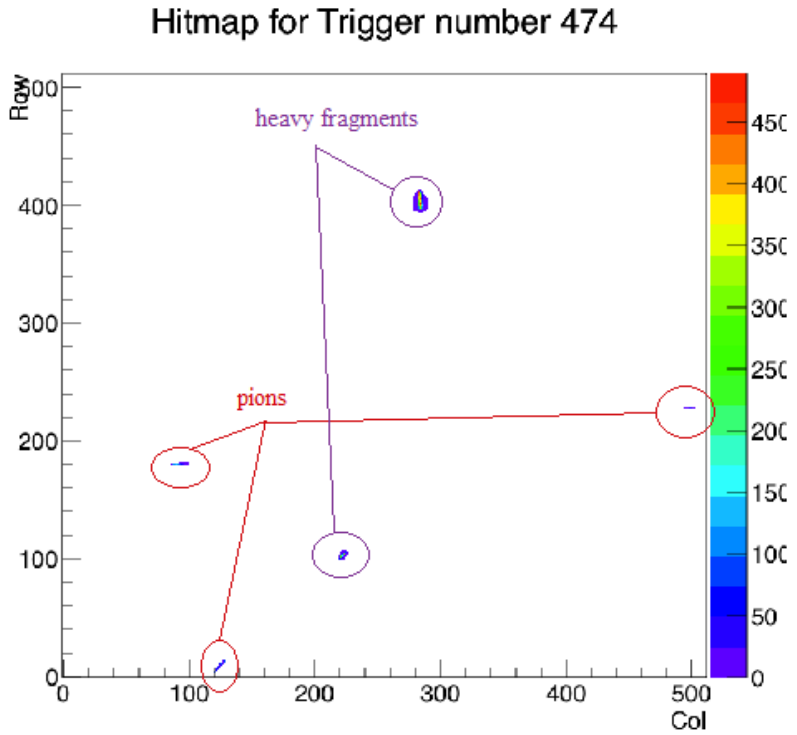

(b) A hitmap for a single isolated, time-stamped event. One can see 5 clusters: the slim tracks are caused by pions, the bigger blotches are heavy fragments.

Figure 3.11: Comparison of a Timepix3 hitmap for a whole run vs. a hitmap for a single annihilation event identified by a time-stamp.

4. Summary, Outlook

This thesis was a contribution to the experiment on antiproton fragmentation at ASACUSA. An overview of the experimental setup was given. A few additions to the beamline were tested. During the beamtime in 2017, some measurements on-site were taken to model the magnetic field for future simulations. A first glimpse at the data taken with Timepix3 is made.

Concerning the new elements of the beamline, first, a cooling method for the Timepix3 detector was successfully tested. The heat generated by Timepix3 can very easily be transported to a back flange via a block of copper and flexible copper bands. Together with a fan providing some extra cooling from outside the Timepix chamber, this keeps the detector and chamber sufficiently cool.
Simulations of the Steerer lens, which is meant to steer and focus the antiproton beam, showed that it would fulfill its purpose as intended. After production, the assembly of the lens was tested and documented. The first usage at CERN showed that steering of the beam worked as planned, but focusing can be improved (FWHM $\sim 25\,\mathrm{mm}$).
To check whether the magnetic field of the Cusp trap prevented better focusing, measurements of the field were performed so it can be included in future simulations. The field was approximated by a magnetic dipole. The results of this fit are in reasonable agreement with the measurements.
A first look at the data recorded by Timepix3 was also made. The data shows very clean signals from individual events, with zero background. Both MIPs and HIPs can be observed and distinguished. Because of the way the Timepix3 data is recorded, a window of time around each time-stamp had to be determined to assign all events in the Timepix3 to their corresponding event in the hodoscope. This window was determined to be $\pm 1\,\mu\mathrm{s}$, it will be used for all further analysis.

Roughly 90 000 annihilation events were recorded by both Timepix3 and the hodoscope in December 2017. Using the data of both detectors, the final goal is to correlate the data, and thus determine the energies and multiplicities of MIPs and HIPs. The analysis of this data is ongoing.

The experiment was continued in 2018, using not only a carbon foil, but also molybdenum and gold foils as annihilation targets.

The final results from this experiment will be very valuable to correctly tune Monte-Carlo simulations of low-energy antiproton annihilation processes.
This is especially relevant data at the moment, as in 2021, after the long shutdown LS2 at CERN, the new decelerator ring ELENA will decelerate antiprotons from the Antiproton Decelerator to even lower energies (from 5.3 MeV down to 100 keV). This facilitates antiproton capture and makes new experiments possible, but also raises the need for correct simulations.

Appendices

A PT100

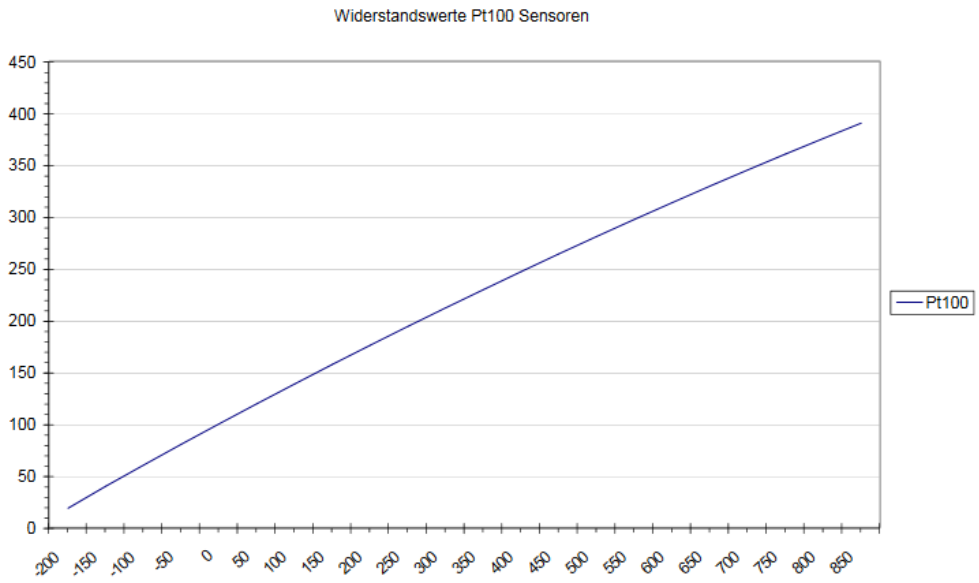

Figure A.1: The characteristic curve of a PT100 resistor. (source: `http://www.pt100.de/pdf/pt100-diag.pdf`)

0 °C correspond to 100 Ω and 25 °C to 110 Ω. In our relevant range of temperatures, this is a (nearly) linear correlation. Thus, the measured values for resistance are converted as follows:

$$T(°\mathrm{C}) = (R - 100) \cdot 2,5$$

B Measured Data Magnetic Field

+X	**+Y**	**+Z**	$\mathbf{B}_{\text{x,sensor}}$ (µT)	$\mathbf{B}_{\text{y,sensor}}$ (µT)	$\mathbf{B}_{\text{z,sensor}}$ (µT)
+X	+Y	-Z	−35	−12	28
-Y	+X	-Z	−18	38	27
-X	-Y	-Z	41	11	32
+Y	-X	-Z	10	−35	34
-X	+Y	+Z	33	−15	−17
+Y	+X	+Z	−19	−32	−19
+X	-Y	+Z	−34	18	−21
-Y	-X	+Z	24	29	−21
+Z	+X	-Y	−5	26	−28
+Z	+Y	+X	−22	−4	−28
+Z	-X	+Y	6	−22	−27
+Z	-Y	-X	29	5	−30
-Z	+Y	-X	26	−21	39
-Z	+X	+Y	−17	−21	40
-Z	-Y	+X	−19	22	37
-Z	-X	-Y	15	26	44
+X	+Z	+Y	−33	−21	−29
-Y	+Z	+X	−23	34	−28
-X	+Z	-Y	37	23	−27
+Y	+Z	-X	24	−30	−26
+Y	-Z	+X	−35	−36	18
+X	-Z	-Y	−34	30	11
-Y	-Z	-X	29	37	−3
-X	-Z	+Y	36	−22	1

Table B.1: The data for calculating the Offset. The first three columns indicate which sensor of the magmeter was aligned with the X-, Y- and Z-axis in space. $B_{x,sensor}$, $B_{y,sensor}$ and $B_{z,sensor}$ are noted as shown by the magmeter, they do not coincide with $B_{x,space}$, $B_{y,space}$ and $B_{z,space}$ (for example, in the second row, $B_{x,sensor}$ shows the Y-component of the magnetic field, as the x-sensor of the device aligns with the y-axis in space)

X (cm)	**Y** (cm)	**Z** (cm)	$\mathbf{B}_{\mathrm{x,sensor}}$ (µT)	$\mathbf{B}_{\mathrm{y,sensor}}$ (µT)	$\mathbf{B}_{\mathrm{z,sensor}}$ (µT)
24.25	−51	276	−14	35	−173
−21.25	−51	276	52	28	−183
19.75	−41.5	250	9	42	−261
−18.25	−41.5	250	52	44	−245
19.75	23.5	241	11	−98	−307
−18.25	23.5	241	62	−96	−295
−21.25	−51	224	107	123	−296
24.25	−51	224	−62	151	−343
30.75	−51	199.5	−126	209	−464
−26.75	−51	199.5	324	172	−321
14.75	−46.5	150	−426	−1094	1049
−9.75	−46.5	150	735	−1080	1053
24.25	−55.5	141	−231	849	−1093
−15.75	−55.5	141	561	825	1040
11.25	26	113.5	−553	−1092	1043
−14.25	26	114	827	−1080	1052
31.75	74	199.5	−37	−309	−327
−30.75	74	208.5	89	−259	−253
24.25	−107	224	1	252	−201
−15.75	−107	224	19	249	−155
24.25	−107	146	−57	662	−381
−15.75	−107	146	277	582	−359
24.25	−51	161	−68	517	−864
−21.25	−51	161	537	468	1044

Table B.2: The measured data of the magnetic field around the hodoscope. X, Y and Z are the distances from the center of the Cusp. $\mathrm{B_{x,sensor}}$, $\mathrm{B_{y,sensor}}$ and $\mathrm{B_{z,sensor}}$ are the components of the magnetic field adjusted for their offsets.

C Python Script

```
import numpy as np
from symfit import Fit, sqrt, variables, parameters,
Model

r_x, r_y, r_z, B_x, B_y, B_z = variables('r_x, r_y, r_z,
                                         B_x, B_y, B_z')
m_x, m_y, m_z = parameters('m_x, m_y, m_z')
m_x.value = 1e-10
m_y.value = 1e-10
m_z.value = -1e-7

model = Model({
        B_x: (10**5)*(3*r_x*(m_x*r_x+m_y*r_y+m_z*r_z)-
              m_x*(r_x**2+r_y**2+r_z**2))/
              ((sqrt(r_x**2+r_y**2+r_z**2))**5),
        B_y: (10**5)*(3*r_y*(m_x*r_x+m_y*r_y+m_z*r_z)-
              m_y*(r_x**2+r_y**2+r_z**2))/
              ((sqrt(r_x**2+r_y**2+r_z**2))**5),
        B_z: (10**5)*(3*r_z*(m_x*r_x+m_y*r_y+m_z*r_z)-
              m_z*(r_x**2+r_y**2+r_z**2))/
              ((sqrt(r_x**2+r_y**2+r_z**2))**5)})

r_xdata = np.genfromtxt('BFeld-data.txt', skip_header=1,
                        usecols=0)
r_ydata = np.genfromtxt('BFeld-data.txt', skip_header=1,
                        usecols=1)
r_zdata = np.genfromtxt('BFeld-data.txt', skip_header=1,
                        usecols=2)
B_xdata = np.genfromtxt('BFeld-data.txt', skip_header=1,
                        usecols=3)
B_ydata = np.genfromtxt('BFeld-data.txt', skip_header=1,
                        usecols=4)
B_zdata = np.genfromtxt('BFeld-data.txt', skip_header=1,
                        usecols=5)

fit = Fit(model, r_x=r_xdata, r_y=r_ydata, r_z=r_zdata,
```

```
            B_x=B_xdata, B_y=B_ydata, B_z=B_zdata)

fit_result = fit.execute()
print(fit_result)
```

References

[1] P. V. Degtyarenko, M. V. Kossov, and H. -P. Wellisch. "Chiral invariant phase space event generator". In: *The European Physical Journal A* 8.2 (July 2000), pp. 217–222. ISSN: 1434-601X. DOI: 10.1007/s100500070108.

[2] T.T. Böhlen et al. "The FLUKA Code: Developments and Challenges for High Energy and Medical Applications". In: *Nuclear Data Sheets* 120 (2014), pp. 211–214. ISSN: 0090-3752. DOI: 10.1016/j.nds.2014.07.049.

[3] B. Andersson, G. Gustafson, and B. Nilsson-Almqvist. "A model for low-pT hadronic reactions with generalizations to hadron-nucleus and nucleus-nucleus collisions". In: *Nuclear Physics B* 281.1 (1987), pp. 289–309. ISSN: 0550-3213. DOI: 10.1016/0550-3213(87)90257-4.

[4] S. Aghion et al. "Detection of low energy antiproton annihilations in a segmented silicon detector". In: *Journal of Instrumentation* 9.06 (June 2014), P06020–P06020. DOI: 10.1088/1748-0221/9/06/p06020.

[5] S. Aghion et al. "Measurement of antiproton annihilation on Cu, Ag and Au with emulsion films". In: *Journal of Instrumentation* 12.04 (Apr. 2017), P04021–P04021. DOI: 10.1088/1748-0221/12/04/p04021.

[6] W. Oelert. "The ELENA Project at CERN". In: *Acta Physica Polonica B* 46 (Jan. 2015), p. 181. DOI: 10.5506/APhysPolB.46.181. arXiv: 1501.05728 [physics.acc-ph].

[7] M. Hori et al. "Buffer-gas cooling of antiprotonic helium to 1.5 to 1.7 K, and antiproton-to-electron mass ratio". In: *Science* 354.6312 (2016), pp. 610–614. DOI: 10.1126/science.aaf6702.

[8] M. Diermaier et al. "In-beam measurement of the hydrogen hyperfine splitting and prospects for antihydrogen spectroscopy". In: *Nature Communications* 8 (June 2017). DOI: 10.1038/ncomms15749.

[9] E. Klempt, C. Batty, and J.-M. Richard. "The Antinucleon-nucleon interaction at low energy: Annihilation dynamics". In: *Phys. Rept.* 413 (2005), pp. 197–317. DOI: 10.1016/j.physrep.2005.03.002. arXiv: hep-ex/0501020 [hep-ex].

[10] O. Chamberlain et al. “Observation of Antiprotons”. In: *Physical Review - PHYS REV X* 100 (Nov. 1955), pp. 947–950. DOI: 10.1103/PhysRev.100.947.

[11] M. Kohno and W. Weise. “Quark model description of low energy proton—antiproton annihilation into two mesons”. In: *Physics Letters B* 152.5 (1985), pp. 303–307. ISSN: 0370-2693. DOI: 10.1016/0370-2693(85)90500-3.

[12] J. Cugnon and J. Vandermeulen. “Antiproton-nucleus interaction”. In: *Ann. Phys. Fr.* 14.1 (1989), pp. 49–87. DOI: 10.1051/anphys:0198900140104900.

[13] J. -P. Burnet et al. “Fifty years of the CERN Proton Synchrotron : Volume 2”. In: (2013). Ed. by Simone Gilardoni and Django Manglunki. DOI: 10.5170/CERN-2013-005. arXiv: 1309.6923 [physics.acc-ph].

[14] M. Hori and J. Walz. “Physics at CERN’s Antiproton Decelerator”. In: *Progress in Particle and Nuclear Physics* 72 (2013), pp. 206–253. ISSN: 0146-6410. DOI: 10.1016/j.ppnp.2013.02.004.

[15] Y. Bylinsky, A. M. Lombardi, and W. Pirkl. “RFQD: A ’Decelerating’ radio frequency quadrupole for the CERN anti-proton facility”. In: *eConf* C000821 (2000). [,554(2000)], TUD05. arXiv: hep-ex/0008030 [hep-ex].

[16] N. Kuroda et al. “Development of a monoenergetic ultraslow antiproton beam source for high-precision investigation”. In: *Phys. Rev. ST Accel. Beams* 15 (2 Feb. 2012), p. 024702. DOI: 10.1103/PhysRevSTAB.15.024702.

[17] N. Kuroda et al. “The ASACUSA CUSP: an antihydrogen experiment”. In: *Hyperfine Interactions* 235.1 (Nov. 2015), pp. 13–20. ISSN: 1572-9540. DOI: 10.1007/s10751-015-1205-1.

[18] P. Delpierre. “A history of hybrid pixel detectors, from high energy physics to medical imaging”. In: *Journal of Instrumentation* 9.05 (May 2014), pp. C05059–C05059. DOI: 10.1088/1748-0221/9/05/c05059.

[19] X. Llopart et al. “Timepix, a 65k programmable pixel readout chip for arrival time, energy and/or photon counting measurements”. In: *Nuclear Instruments and Methods in Physics Research Section A: Accelerators, Spectrometers, Detectors and Associated Equipment* 581.1 (2007). VCI 2007, pp. 485–494. ISSN: 0168-9002. DOI: 10.1016/j.nima.2007.08.079.

[20] T. Poikela et al. “Timepix3: a 65K channel hybrid pixel readout chip with simultaneous ToA/ToT and sparse readout”. In: *Journal of Instrumentation* 9.05 (May 2014), pp. C05013–C05013. DOI: 10.1088/1748-0221/9/05/c05013.

[21] J. Visser et al. “SPIDR: a read-out system for Medipix3 & Timepix3”. In: *Journal of Instrumentation* 10.12 (Dec. 2015), pp. C12028–C12028. DOI: 10.1088/1748-0221/10/12/c12028.

[22] A. Capon. “Construction of a Scintillating Hodoscope Detector for Measurements on the Hyperfine Structure of Antihydrogen”. Master’s Thesis. Universität Wien, 2016.

[23] C. Sauerzopf. “The ASACUSA Antihydrogen Detector: Development and Data Analysis”. PhD Dissertation. Technische Universität Wien, 2016.

[24] M. Fleck. “The Development and Implementation of a Fibre Detector and Advanced Data Acquisition for the ASACUSA Antihydrogen Detector”. Master’s Thesis. Technische Universität Wien, 2018.